THE ASTROPHYSICAL JOURNAL, 404:124–143, 1993 February 10

OBSERVATIONS OF THE GASEOUS GALACTIC HALO TOWARD 3C 273 WITH THE GODDARD HIGH RESOLUTION SPECTROGRAPH[1]

BLAIR D. SAVAGE AND LIMIN LU
Washburn Observatory, University of Wisconsin, 475 N. Charter Street, Madison, WI 53706
RAY J. WEYMANN AND SIMON L. MORRIS
Observatories of the Carnegie Institution of Washington, 813 Santa Barbara Street, Pasadena, CA 91101
AND
RONALD L. GILLILAND
Space Telescope Science Institute, 3700 San Martin Drive, Baltimore, MD 21218
Received 1992 June 16; accepted 1992 June 16

ABSTRACT

We present an analysis of observations of 24 absorption lines produced near zero redshift by Milky Way disk and halo gas along the sight line to 3C 273. The observations were obtained with the intermediate-resolution mode of the Goddard High Resolution Spectrograph (GHRS) using the large entrance aperture. The spectral spread function has FWHM ~ 20 km s^{-1} and broad wings. The species detected include C II, C II*, C IV, O I, N V, Mg II, Si II, Si IV, S II, Mn II, Fe II, and Ni II. The O I line is contaminated by Earth atmospheric emission, and one of the Si IV doublet lines is contaminated by what is likely an intergalactic H I Lyman-α line. The set of absorption lines provides information about neutral and highly ionized gas in the Galactic disk and halo. The data permit estimates of reliable column densities and depletions for Si II, S II, Mn II, and Ni II. A value of $N(H\ \text{I})$ is obtained from profile fitting to the Faint Object Survey Lyman-α measurement of Bahcall et al. (1991a). We analyze the GHRS data using standard curve-of-growth techniques and the apparent optical depth method and find that S based on S II is overabundant by 0.16 dex, while Si, Mn, and Ni have modest depletions (-0.67 to -0.81 dex) which are representative of the low-density interstellar medium. The suggested S overabundance is probably due to the presence of substantial amounts of S II in the warm ionized gas toward 3C 273. The presence of the ionized gas probably also influences the results for Si, Mn, and Ni. An estimate of the column density of C II* yields information about the cooling rate per nucleon in the gas toward 3C 273. The cooling rate is 7 times lower than the average found in the Galactic disk. Reliable column densities are obtained for Si IV, C IV, and N V. The amount of highly ionized gas toward 3C 273 is compared with that found for other sight lines to Galactic stars and to stars in the LMC and SMC. The amount of highly ionized gas perpendicular to the Galactic plane is about 2–3 times that seen toward the LMC and SMC. The highly ionized gas (including recent observations of O VI by Davidsen et al. 1992 seems best explained as being associated with the cooling flow of a Galactic fountain with additional contributions to the absorption from gas associated with the energetic events that produced Galactic radio loops I and IV. The data provide kinematical information about gas motions along an extended path through the halo. The high-ionization lines have average velocities approximately 10 km s^{-1} more negative than the weaker low-ionization lines, suggestive of inflow of hot gas along this high-latitude sight line. The very strongly saturated lines for Fe II, Mg II, Si II, and C II exhibit full extents at half-absorption depths ranging from ~ 120 km s^{-1} up to ~ 150 km s^{-1}. These lines are evidently tracing a high-velocity dispersion phase of the gas toward 3C 273 that is apparent in H I 21 cm emission-line measurements. High-velocity gas absorption-line components with 100 km s^{-1} $< |v| <$ 1000 km s^{-1} are not evident in any of the profiles for the strong low-ionization species or for the highly ionized species. The GHRS absorption-line equivalent widths for all detected species are compared with the measurements for other extragalactic sight lines, including those to the LMC, the SMC, and H1821+643. In the case of the strong low-ionization lines, the absorption-line equivalent widths for 3C 273 are intermediate to those for the SMC sight line and the LMC and H1821+643 sight lines. The strong low-ionization lines mostly measure the kinematical conditions along the sight line to each object. The high-ionization lines are less saturated and mostly provide a measure of the column density, which is greater toward 3C 273 than for the other paths. The 3C 273 Milky Way disk and halo absorption-line data are compared with measurements for QSO damped Lyman-α absorption-line systems and found to be similar. The low-ionization lines compared are strongly saturated. Therefore, the correspondence implies a similarity of the kinematical behavior of the turbulent phases of the different absorbing systems and does not necessarily imply similar elemental abundances.

Subject headings: Galaxy: halo — Galaxy: kinematics and dynamics — ISM: abundances — quasars: individual (3C 273)

1 Based on observations with the NASA/ESA *Hubble Space Telescope*, obtained at the Space Telescope Science Institute, which is operated by the Association of Universities for Research in Astronomy, Inc., under NASA contract NAS5-26555.

1. INTRODUCTION

The first high-resolution ultraviolet absorption-line measurements of hot stars in the Large and Small Magellanic Clouds provide unique insights about interstellar gas situated at large distances away from the Galactic plane (Savage & de Boer 1979, 1981). Those early observations with the *International Ultraviolet Explorer* (*IUE*) satellite were followed by a number of absorption-line studies with the *IUE* of brighter stars situated in the low halo of the Milky Way at distances $|z|$ away from the Galactic plane of typically less than 3 kpc (Pettini & West 1982; Savage & Massa 1987; Danly 1989). These measurements and others at optical and radio wavelengths have revealed that the gaseous atmosphere (gaseous halo) of the Galaxy is an extremely interesting region. It contains cold, warm, and hot gas, with the different phases having different distributions away from the Galactic plane (see Savage 1988 for a review). The very existence of gas at large distances from the Galactic plane may involve such energetic processes as Galactic fountains and chimneys, or the support of the gas might be provided by the pressure from magnetic fields and streaming cosmic rays (see Spitzer 1990 for a review).

The small collecting area of the *IUE* combined with relatively high detector noise at low signal levels has made it very difficult to obtain additional high-resolution absorption-line measurements through the halo of the Milky Way toward objects with distances away from the Galactic plane exceeding about 3 kpc. By taking extraordinary measures, Burks et al. (1991) have obtained *IUE* absorption-line measurements of selected Milky Way halo lines in the spectrum of 3C 273 with signal-to-noise ratios from about 3 to 10. The Burks et al. data are comparable to those obtained by deBoer & Savage (1983, 1984) of several UV-bright stars in the Galactic globular clusters M13 and M3 at $|z| = 4.1$ and 10 kpc, respectively. Unfortunately, *IUE* spectra of faint objects often contain spurious features which are much stronger than the apparent noise.

The brightest QSO, 3C 273, was the obvious first choice for investigating the capabilities of the intermediate-resolution mode of the Goddard High Resolution Spectrograph (GHRS) for obtaining spectra of extragalactic sources in the far-UV. The first paper announcing the GHRS 3C 273 absorption-line results (Morris et al. 1991) reported the discovery of the low-redshift analog of the Lyman-α forest with the number of low-redshift absorption lines being 5–10 times larger than expected on the basis of a simple extrapolation of the evolutionary trends found in ground-based data (also see Bahcall et al. 1991a). The GHRS measurements also revealed the presence of very strong UV absorption lines produced by Milky Way disk and halo gas, including the detection of N v, an important diagnostic of hot interstellar gas with $T \sim 2 \times 10^5$ K.

The purpose of this paper is to provide an analysis of the 24 absorption lines found in the GHRS intermediate-resolution spectrum of 3C 273 that we attribute to gas in Milky Way disk and halo. Our paper is organized as follows: A brief discussion of the observations and calibrations is found in § 2. In § 3 we present an overview of what is known about the nature of the interstellar sight line to 3C 273 based on information from the literature. This is important because any sight line through the halo will be influenced by local and distant Galactic structures. The GHRS results are presented in § 4 and discussed in § 5. The presentation is ordered according to the level of ionization of the species seen. Thus there are results for neutral and weakly ionized gas as traced by C II, C II*, O I, Mg II, Si II, S II, Mn II, Fe II, and Ni II and results for highly ionized gas as traced by C IV, N V, and Si IV. A summary of our study is found in § 6.

2. OBSERVATIONS, CALIBRATIONS, AND MEASUREMENTS

Brief discussions of how the 3C 273 GHRS observations were obtained and initially reduced are found in Morris et al. (1991) and Gilliland et al. (1992). Detailed discussions of the data acquisition and the more recent efforts to process and calibrate the spectra using updated calibration software and reference files are found in Brandt et al. (1993). Thus, our discussion here will be relatively brief and limited to those aspects of the data set which involve absorption produced by the Milky Way. A detailed description of the GHRS instrument and its preflight characteristics is found in Duncan (1992). The results of the in-flight science verification program are presented in great detail by Ebbets (1992).

Table 1 lists the GHRS intermediate-resolution observations of 3C 273 which were obtained 1991 February 23 (UT). We list the *Hubble Space Telescope* (*HST*) data archive identification number, the grating, the spectral region covered by each integration with the 500 diodes of the Digicon detector, the integration time, and the Milky Way ions detected in each integration. All measurements were obtained with 3C 273 positioned in the $2'' \times 2''$ large science aperture (LSA). The spectrum and internal background were sampled using Digicon substep pattern 5, which provides quarter-diode spectrum sampling and also samples the background above and below the spectrum with approximately 6.3% of the integration time. To reduce photocathode fixed-pattern noise and diode-to-diode sensitivity variations, the scanning was performed using four-diode comb-addition and FP split = 4. The comb-addition averages the detected spectrum over four Digicon detector diodes, while the FP-split sequence breaks each spectral integration into four parts between which the grating is moved by an amount corresponding to approximately five Digicon diodes. By aligning and combining the four individual FP-split exposures, photocathode fixed-pattern noise is reduced. The on-board Doppler compensation to correct for spacecraft motion was enabled during all observations. Special wavelength calibration measurements were obtained for the three grating setup positions identified in Table 1 using the platinium-neon lamp aboard the spacecraft. The wavelength calibrations for the other observations were established with reference to standard calibrations (called DEFCAL) which are associated with platinum-neon lamp measurements obtained in order to center the electron image of the spectrum on the diode array.

The results we report are based on spectra of 3C 273 processed at the University of Wisconsin using the standard calibration software package (CALHRS) available to us through the GHRS computing facility at the Goddard Space Flight Center. The calibration files and procedures are equivalent to those implemented in the Space Telescope Science Institute's Routine Science Data Processing (RSDP) files as of 1992 January 1. These files are preserved in the *HST* data archive. The processing includes converting raw counts to count rates, correcting for diode nonuniformities, paired pulse events, and spectrograph vignetting. The individual FP-split spectra are aligned and merged using the standard merge routine to form spectra with four samples per diode. See Brandt et al. (1993) for a discussion of the different FP-split spectrum merging options. The combined effects of particle radiation and scattered light background are removed using an average of

TABLE 1

GHRS Intermediate-Resolution Large-Aperture Measurements

Identification[a]	Grating	Spectral Range (Å)	Exposure Time[b] (s)	Species Detected[c]
Z0GU010CM[d] ...	G160M	1521.7–1558.0	1400.26	Si II, C IV
Z0GU010EM	G160M	1389.0–1425.8	1938.82	Si IV
Z0GU010GM ...	G160M	1359.0–1395.9	1938.82	Ni II, Si IV
Z0GU010IM	G160M	1326.7–1363.6	1938.82	C II, C II*
Z0GU010KM ...	G160M	1296.3–1333.3	1938.82	O I, Si II
Z0GU010MN ...	G160M	1265.7–1302.7	1938.82	None
Z0GU010OM ...	G160M	1234.6–1271.8	2908.22	N V, S II, Si II
Z0GU010SM[d] ...	G200M	1773.1–1814.8	969.41	Si II
Z0GU010VM[d] ...	G270M	2776.2–2823.4	969.41	Mg II
Z0GU010WM ...	G270M	2570.9–2619.0	969.41	Mn II, Fe II

[a] *HST* data archive identification.
[b] Total exposure time, including ~6.3% of the time spent on obtaining backgrounds.
[c] Only ISM lines are listed. Intergalactic absorption features are given in Brandt et al. 1993.
[d] Special Pt-Ne calibration lamp spectra were obtained as part of these measurements.

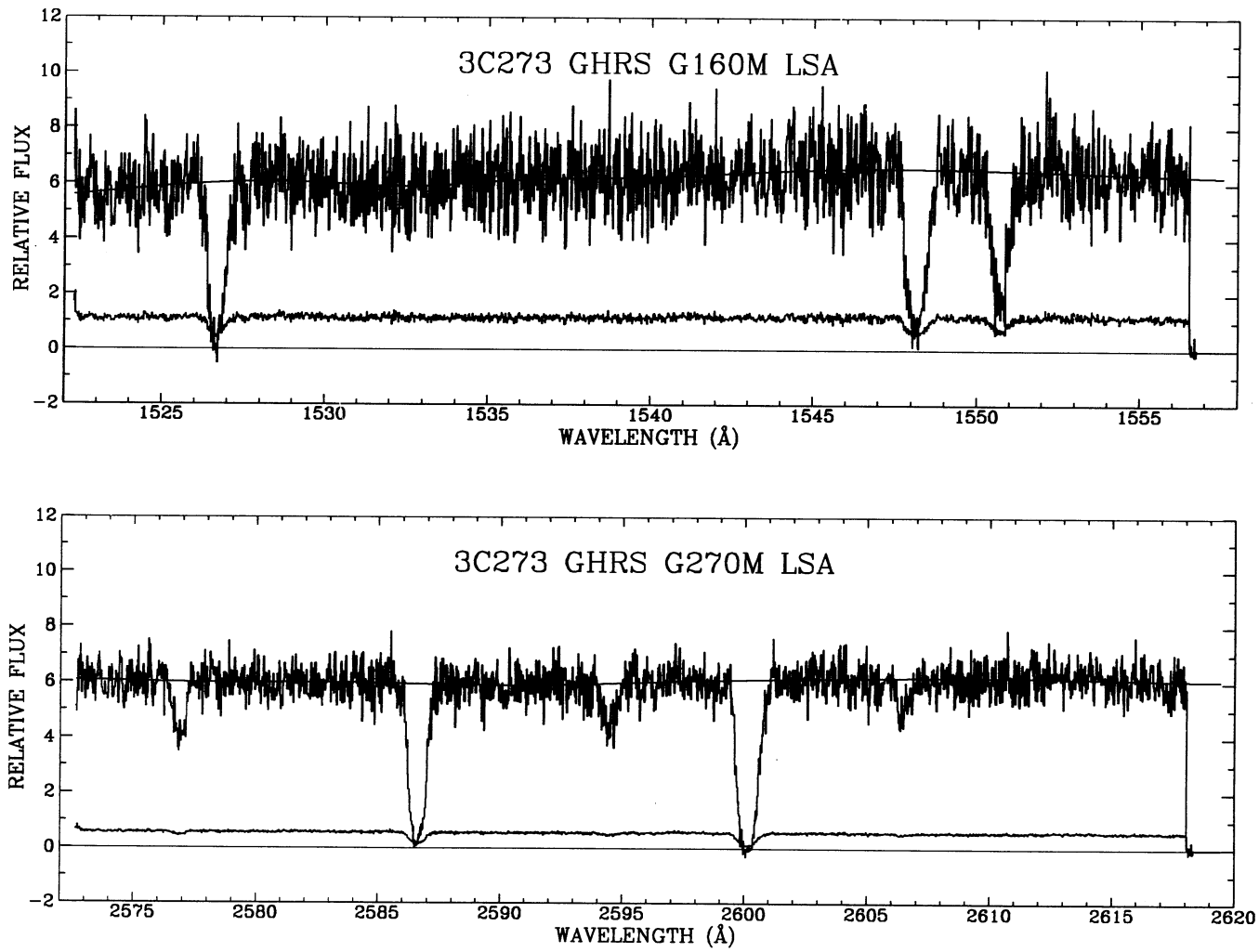

FIG. 1.—GHRS Digicon 500 diode array spectra of the G160M measurement from 1521.7 to 1558.0 Å (*top*) and of the G270M measurement from 2570.9 to 2619.0 Å (*bottom*). Relative flux is plotted against heliocentric wavelength. The spectra shown are with the full sampling of four substeps per diode width. The obvious spectral features are due to absorption by disk and halo gas in the Milky Way and include Si II λ1526.707 and C IV λλ1548.195 1550.770 in the upper spectrum, and Mn II λλ2576.877, 2594.499, 2606.462 and Fe II λλ2586.650, 2600.173 in the lower spectrum. The 1 σ statistical noise as a function of wavelength is shown as the lower curve in each panel. Our fitted continuum is also shown superposed on each spectrum.

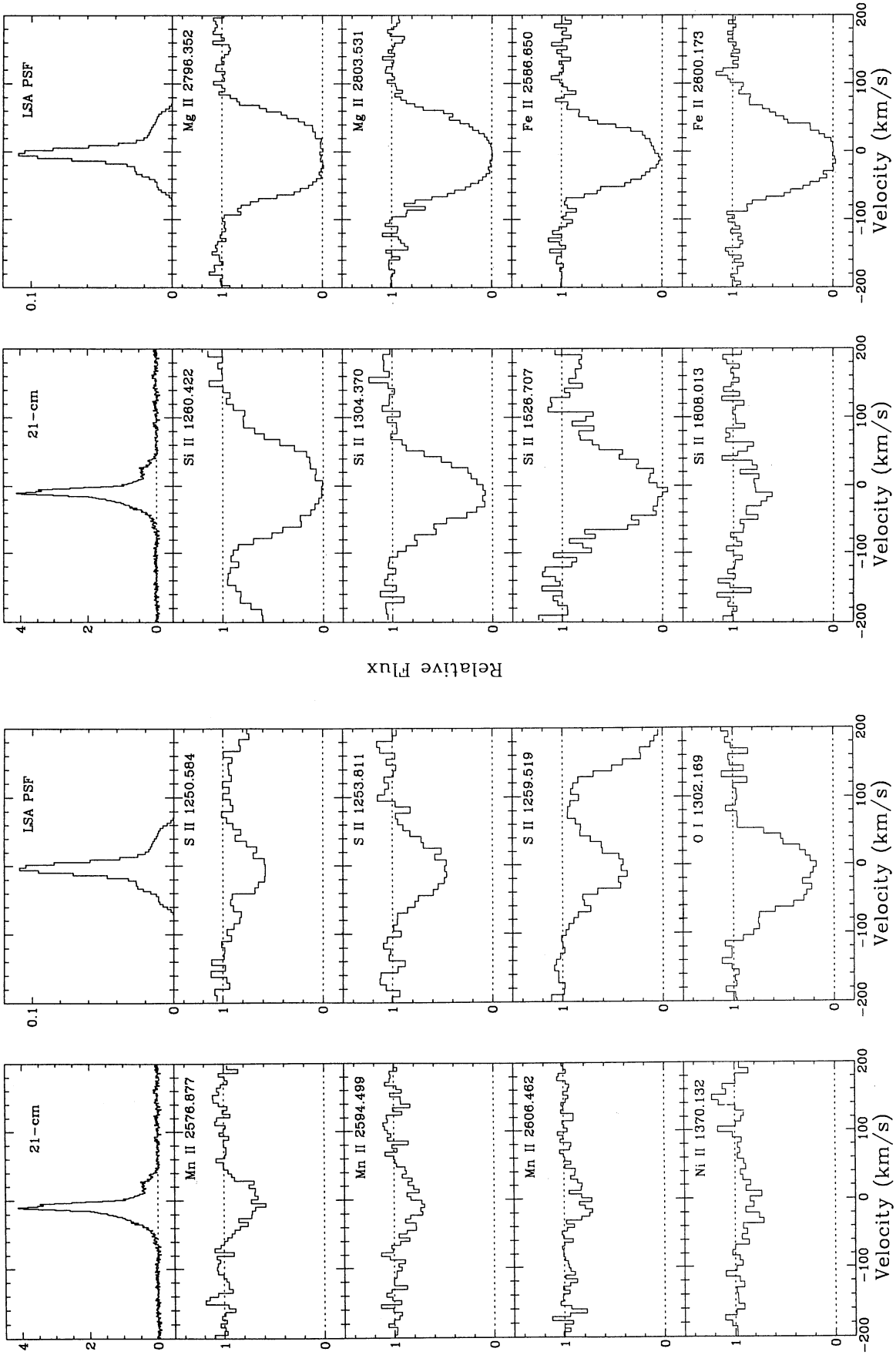

FIG. 2.—Continuum normalized relative intensity vs. heliocentric velocity in kilometers per second, shown for all Galactic absorption lines detected in the GHRS intermediate-resolution data for the sight line to 3C 273. The dashed lines trace the continuum. Additional information about the detected ions is found in Table 2. In several cases absorption by other species influences the appearance of the plots. These include the plot for S II λ1250.584, which reveals an intensity depression for $v > 150$ km s^{-1} due to an intergalactic H I line centered at 1251.45 Å (Morris et al. 1991); the plots for S II λ1259.811 include a contribution from Si II λ1260.422 for $v > 100$ km s^{-1}; and the plot for Si II λ1260.422 is affected by S II λ1259.519 for $v < -150$ km s^{-1}. The O I λ1302.169 absorption-line measurement is filled in by an unknown amount of atmospheric O I emission. The Si IV λ1393.775 line is contaminated by intergalactic Lyman-α absorption (see § 4.4). At the top of each panel the H I 21 cm emission-line profile (antenna temperature vs. heliocentric velocity) from Lockman & Savage (1993) is shown. In addition, the GHRS spectroscopic spread function for the G160M grating mode operating with the LSA is illustrated.

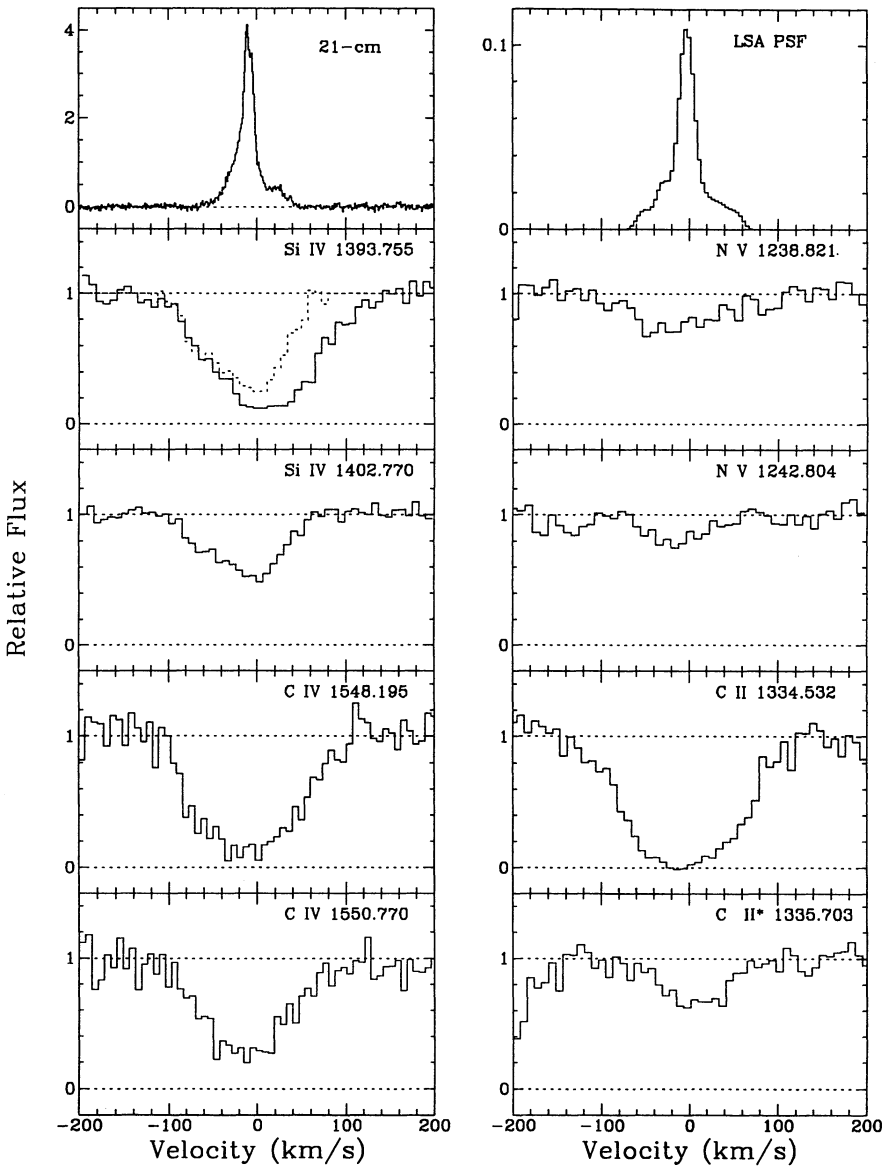

FIG. 2—*Continued*

the diode-array measurements obtained above and below the spectral integrations.

The signal-to-noise ratio in the resulting quarter-diode sampled spectra was approximately 9, except for the measurements with G270M, where the value is about 15. Sample full-array spectra are shown in Figure 1 for the 1522–1556 Å region with G160M and the 2573–2616 Å region with G270M. Since the data are oversampled because of the use of the LSA (see below), we have based our interstellar line analysis on spectra with adjacent quarter-diode substeps averaged to produce final spectra with typical signal-to-noise ratios of 13–20. Line profile plots showing continuum normalized intensity versus heliocentric velocity for all the interstellar lines detected are illustrated in Figure 2.

The accuracy of the wavelength calibration is affected by the use of the LSA, since small differences in the position of 3C 273 in the aperture from measurement to measurement will introduce velocity shifts in the spectra recorded. We estimate that the processed spectra have a 1 σ velocity error of approximately 10 km s^{-1}, which corresponds to a width of somewhat less than one diode.

Because of the spherical aberration of the *HST* primary mirror, the image of an object in the LSA consists of a sharp core with broad wings. This causes the GHRS intermediate-resolution mode LSA observations to have a spectral spread function with a sharp core and broad wings as illustrated in Figure 2 for the G160M mode. The core contains $\sim$40% of the area of the spread function and has a FWHM of approximately 20 km s^{-1}. The broad wings contain $\sim$60% of the area and extend approximately $\pm$70 km s^{-1}. Attempts to apply deconvolution techniques to GHRS intermediate- and low-resolution data for 3C 273 are found in Morris et al. (1991), Gilliland et al. (1992), and Brandt et al. (1993). While the techniques were quite successful in improving the resolution of the high signal-to-noise low-resolution data, the improvement for the intermediate-resolution data with modest signal-to-noise

ratio was not impressive. Most of our analysis will be on the data before deconvolution, with occasional reference to the deconvolved spectra presented by Brandt et al. (1993). We will need to be constantly aware that the measurements were obtained with a spectroscopic spread function that introduces a considerable amount of blurring.

In order to measure absorption lines, a continuum must be established first for each spectrum. This is done according to the following procedures. A spectrum is first divided into many segments, with each segment containing typically ~ 100 data points corresponding to the width of 50 diodes. The mean flux value and standard deviation are then computed for each of those segments that contains no obvious absorption features. Data points which deviate from the mean flux by more than 2.5 times the standard deviation are excluded, and new mean flux value and standard deviation are computed. The process is repeated until no more data points can be excluded. A cubic spline function is then fitted to the mean flux values located at the central wavelength of the segments, which is taken as the continuum. Absorption features are then searched for against the determined continuum using an automated computer program. The program first identifies each continuous depression below the continuum as an absorption feature, and computes the equivalent width of the feature by direct integration. The program also computes the error in the equivalent width, σ_p, that is due to photon counting uncertainties from the noise spectrum. To estimate the error in the equivalent width, σ_c, that is due to continuum placement uncertainty, a smoothed version of the noise spectrum is first created by removing strong downward excursions due to absorption features or strong upward excursions due to events, such as cosmic-ray hits. The error σ_c is then taken as the difference in the equivalent width of the absorption feature incurred by raising or lowering the entire continuum by the amount of 0.4 times the smoothed noise spectrum. The total error in the equivalent width, σ_W, is then the sum of σ_p and σ_c in quadrature. Numerical simulations have shown that this procedure provides a reasonable estimate of the uncertainty in equivalent width measurements (Sembach, Savage, & Massa 1991). A specialized program is then used to measure the equivalent widths more accurately by directly integrating over some specified integration velocity ranges. The program can also be used to decompose blended lines. Only absorption features with equivalent widths exceeding 3 σ_W are retained in the line list. The equivalent widths of all Galactic absorption lines satisfying the above criterion are given in Table 2.

TABLE 2

EQUIVALENT WIDTH MEASUREMENTS

Ion	λ[a] (Å)	log λf	v_-[b] (km s^{-1})	v_+[b] (km s^{-1})	$\langle v_{\rm helio} \rangle$[c] (km s^{-1})	$W_\lambda \pm \sigma$ (Å)
C II	1334.532	2.232	− 140	+ 110	− 8	0.671 ± 0.020
C II*	1335.703	2.232	− 80	+ 70	+ 2	0.142 ± 0.023
C IV	1548.195	2.470	− 110	+ 110	− 9	0.604 ± 0.035
C IV	1550.770	2.121	− 110	+ 110	− 9	0.455 ± 0.043
N V	1238.821	2.289	− 110	+ 70	− 15	0.126 ± 0.023
N V	1242.804	1.988	− 110	+ 70	− 17	0.071 ± 0.024
O I	1302.169	1.804	− 110	+ 100	− 18	0.395 ± 0.021[d]
Mg II	2796.352	3.234	− 100	+ 100	− 5	1.166 ± 0.026
Mg II	2803.531	2.933	− 100	+ 100	− 5	1.121 ± 0.027
Si II	1260.422	3.104	− 140	+ 140	− 1	0.600 ± 0.022
Si II	1304.370	2.284	− 100	+ 100	− 14	0.407 ± 0.019
Si II	1526.707	2.546	− 100	+ 100	− 5	0.596 ± 0.029
Si II	1808.013	1.000	− 80	+ 70	− 9	0.136 ± 0.043
Si IV	1393.755	2.855	− 110	+ 70	− 17	0.356 ± 0.017[e]
Si IV	1402.770	2.554	− 110	+ 70	− 16	0.215 ± 0.017
S II	1250.584	0.834	− 100	+ 80	− 10	0.160 ± 0.020
S II	1253.811	1.135	− 100	+ 80	− 5	0.211 ± 0.020
S II	1259.519	1.311	− 100	+ 80	− 8	0.236 ± 0.019
Mn II	2576.877	2.956	− 80	+ 70	− 5[f]	0.185 ± 0.034
Mn II	2594.499	2.847	− 80	+ 70	− 6[f]	0.159 ± 0.036
Mn II	2606.462	2.701	− 80	+ 70	− 2[f]	0.118 ± 0.037
Fe II	2586.650	2.223	− 100	+ 100	− 6[f]	0.783 ± 0.030
Fe II	2600.173	2.765	− 100	+ 100	− 3[f]	1.001 ± 0.025
Ni II	1370.132	2.254	− 80	+ 70	− 5	0.084 ± 0.025

[a] Rest-frame, vacuum wavelength from Morton 1991.

[b] v_- and v_+ give the velocity range within which the equivalent widths and column densities are obtained.

[c] Average heliocentric velocity for the absorption.

[d] Uncorrected for geocoronal emission.

[e] After deblending (see § 4.4).

[f] The velocities for the Mn II and Fe II lines are shifted by approximately +17 km s^{-1} from those listed by Morris et al. 1991.

3. THE GALACTIC SIGHT LINE TO 3C 273

A considerable body of data now exists which indicates that our view of the Galactic halo will be influenced by the observation direction. For example, approximately 11% or more of the sky is covered by high-velocity clouds with velocities referenced to the local standard of rest $|v_{LSR}| > 100$ km s^{-1} (Wakker 1991). The fraction covered by intermediate-velocity gas with $100 > |v_{LSR}| > 50$ km s^{-1} is considerably larger. H I shells and supershells are found in some directions and not others (Heiles 1979). Interstellar absorption-line studies with *IUE* of stars with $|z|$ up to about 2 kpc indicate that the Galactic distribution of highly ionized gas as traced by Si IV, C IV, and N V is quite inhomogeneous (Savage & Massa 1987; Sembach & Savage 1992). The processes creating regions of highly ionized gas away from the Galactic plane may extend over spatial scales which are large enough to introduce inhomogeneities.

The Galactic sight line to 3C 273 is the direction $l = 289.°95$ and $b = 64.°38$, which complements the directions to the LMC ($l = 279°$; $b = -33°$) and SMC ($l = 302°$; $b = -45°$) for which *IUE* has provided high-quality interstellar absorption-line data through the entire halo (Savage & de Boer 1981; Fitzpatrick & Savage 1983; Savage et al. 1989; Sembach & Savage 1992).

The sight line to 3C 273 extends into the halo through the local interstellar medium and the edges of radio loops I and IV, which are seen in radio continuum radiation (Berkhuijsen 1971), 21 cm emission structures such as the North Polar Spur (Coulomb, Poppel, & Heiles 1980; Heiles et al. 1980), and diffuse soft X-rays (McCammon et al. 1983). The C-band X-ray emission in the general direction of 3C 273 reveals what appears to be a ridge of emission where the excess emission in the ridge is about twice that seen in adjacent regions. These local structures are probably tracing the regions of hot gas created by past supernova explosions. Since this kind of structure is invoked in some theories for the origin of Galactic halo gas (i.e., Galactic fountain models) we should not be too surprised that we will occasionally need to view the halo through such structures. In fact, it is difficult to avoid the structure, since it has a diameter of about 120° and covers approximately a fourth of the entire sky. The radius and central distance of the structure are estimated to be 115 and 130 pc, respectively (Berkhuijsen 1973). In interpreting the 3C 273 absorption-line results, we will need to recognize that some portion of the observed absorption may arise in these local structures. Perhaps the sight line to 3C 273 is providing us with the unique opportunity to study the processes that initiate the Galactic fountain. Iwan (1980) has developed a model for the North Polar Spur as an old supernova remnant which has been reheated by a second supernova shock, with loop IV being the candidate for the radio shell of the reheating remnant. The sketch of the model shown by Iwan (1980) suggests that loop I may extend ~200 pc from the Galactic plane, while loop IV may extend ~400 pc. The model suggests the birth of a "Galactic chimney." In Iwan's model the interiors of loop I and loop IV are believed to contain gas with $T \sim (1\text{–}3) \times 10^6$ K. Such gas is too hot to produce the highly ionized absorption lines we are able to probe in the UV. However, the general region, and in particular the interface between the hot gas and cooler boundaries of the cavities, might contain the intermediate-temperature gas detected in the absorption-line data.

The high-quality Ca II optical interstellar absorption-line measurements for 3C 273 obtained by Meyer & Roth (1991) at 14 km s^{-1} resolution reveal two strong components with $v_{helio} = -23$ and $+23$ km s^{-1} having column densities of 2.1×10^{12} and 1.9×10^{12} cm^{-2}, respectively. The profiles they show also suggest weaker components near approximately -50, -10, and $+50$ km s^{-1}. Meyer & Roth (1991) also obtained absorption-line measurements for the sight line to the extragalactic supernova SN 1991T, which lies only 1.°4 from 3C 273. Those data reveal low-velocity absorption similar to that seen toward 3C 273 but also show high-velocity Ca II absorption components near $v_{helio} = -89$, 213, and 261 km s^{-1}. Evidently, the inhomogeneous nature of the sky in this direction exists over relatively small angular scales. The high-velocity absorption detected by Meyer & Roth may occur in the halo or may be associated with those energetic events that have created radio loops I and/or IV.

Blades & Morton (1983) have reported Galactic Na I D1 and D2 absorption toward 3C 273 at a resolution of 24 km s^{-1} showing components near $v_{helio} = -12$ and $+24$ km s^{-1}. For the D1 line the feature at positive velocities has about twice the equivalent width of the one at negative velocities. These Na I measurements do not reveal absorption near the Ca II feature at -23 km s^{-1}. The Ca II and Na I data together indicate the presence of at least three principal absorptions with differing values of the ratio of Ca II to Na I.

To provide an aid for the interpretation of the UV absorption-line data, we show in Figure 2 the H I 21 cm emission-line measurement of Lockman & Savage (1993) for the sight line to 3C 273 obtained with the NRAO 43 m radio telescope with a velocity resolution of 1 km s^{-1}. The data were corrected for antenna sidelobe contamination by using the procedure discussed in Lockman, Jahoda, & McCammon (1986). The radio measurements record H I emission over the 21′ (FWHM) beam of the antenna, while the UV absorption refers to absorption over the extremely small solid angle of 3C 273 itself. The H I profile can be modeled crudely with three Gaussian components near $v_{helio} = -25$, -8, and $+19$ km s^{-1}, consistent with the Ca II/Na I observations. The radio data also show extensions of detectable emission to -55 and $+45$ km s^{-1} and no evidence for high-velocity H I with 70 km s^{-1} $< |v_{LSR}| <$ 200 km s^{-1} with a column density limit of approximately 2×10^{18} cm^{-2}. The total column density of H I in the direction of 3C 273 obtained from the 21 cm emission and an assumed spin temperature of 1000 K is $N(\text{H I}) = 10^{20.23 \pm 0.015}$ atoms cm^{-2} (Lockman & Savage 1993). Changing the spin temperature to 75 K increases the column density by approximately one-half of the error quoted. The column density from the 21 cm data agrees with the value of $N(\text{H I}) = 10^{20.1 \pm 0.2}$ atoms cm^{-2} determined from the GHRS low-resolution Lyman-α absorption-line measurements reported by Morris et al. (1991). The GHRS column density is quite uncertain because of the substantial contamination from geocoronal H I Lyman-α emission. It is possible to obtain a more accurate value from the Lyman-α absorption from the less contaminated Faint Object Spectrograph (FOS) measurements reported by Bahcall et al. (1991a). Using those data and the profile reconstruction technique of Bohlin (1975), we derive $N(\text{H I}) = 10^{20.22 \pm 0.08}$ atoms cm^{-2}. This new value of N(H I) from the FOS data will be used in the sight-line abundance discussions of §§ 4 and 5.

The velocity of the strong H I emission ($v_{helio} = -8$ km s^{-1}) agrees with the velocity of Na I absorption noted above, while

Ca II absorption is weak where the H I emission is strong. This behavior is likely due to the extreme depletion of Ca typically found for low-velocity gas in the Galactic disk (Hobbs 1974). Such an effect likely influences the metal lines we detect in the UV measurements.

4. RESULTS

Line profile plots illustrating continuum normalized intensity versus heliocentric velocity for all the detected Milky Way lines are shown in Figure 2. For the direction to 3C 273, the conversion between LSR and heliocentric velocity is given by $v_{\rm LSR} = v_{\rm helio} + 2.3$ km s^{-1}. Table 2 provides values of rest wavelength, λ (Å), and log (λf) from Morton (1991) for all detected lines. The species detected include tracers of neutral and weakly ionized gas as revealed by C II, C II*, O I, Mg II, Si II, S II, Mn II, Fe II, and Ni II, along with tracers of highly ionized gas as revealed by Si IV, C IV, and N V. In one case, Si IV λ1393.755, the Milky Way absorption is blended with an intergalactic Lyman-α line (see § 4.4), while for O I λ1302.169 the blending is with Earth atmospheric O I emission.

Milky Way UV absorption lines of interest which might be expected to be found with the detection threshold of approximately 0.06–0.08 Å (3 σ) but are not seen include Ni II λ1317.217, C I λ1277.2454, and the (5, 0) band of CO λ1392.529. the absence of the Ni II λ1317.217 line with a 3 σ limit of about 0.07 Å is puzzling. Morton (1991) lists values of log (λf) = 2.284 and 2.254 for Ni II $\lambda\lambda$1317.217 and 1371.132, respectively. The GHRS measurements do reveal the presence of Ni II λ1371.132 with $W_\lambda = 0.084 \pm 0.025$ Å. A line near 1317.08 Å with $W_\lambda = 0.292$ Å was seen by Bahcall et al. (1991a) in their λ1371.132 with $W_\lambda = 0.084 \pm 0.025$ Å. A line near 1317.08 Å with $W_\lambda = 0.292$ Å was seen by Bahcall et al. (1991a) in their FOS spectra and identified as intergalactic Lyman-α absorption. A much weaker line near that wavelength is seen in the GHRS deconvolved low-resolution observations shown in Figure 1 of Morris et al. (1991). The reliability of the relative values of log (λf) for the two Ni II lines can be inferred from the interstellar absorption-line data presented by Morton (1975) for the sight line to ζ Ophiuchi. For the Ni II 1370.136 Å line he reports $W_\lambda = 0.0197 \pm 0.0057$ Å and also reports an unidentified line at 1317.140 Å with $W_\lambda = 0.019$ Å. Evidently, Morton's unidentified line is Ni II λ1317.217, and it has nearly the same strength as the longer wavelength Ni II line. Therefore, the *Copernicus* satellite data imply that the values of log (λf) for the two Ni lines are similar, in agreement with the values of log (λf) listed above. The weakness of the Ni II lines toward ζ Oph are the result of the extremely large gas-phase depletion found for Ni in normal diffuse clouds. We conclude that the features seen near 1317.2 and 1371.1 Å in some of the GHRS data are probably produced by Ni II and that a positive noise excursion has caused the absence of the 1317.2 Å feature in the GHRS G160M measurement. Noise may have contributed to the 0.292 Å feature near 1317.08 Å seen by Bahcall et al. (1991a). A feature that strong is incompatible with the GHRS intermediate-resolution data. In comparing GHRS and FOS results we note that Bahcall et al. (1991b) have found that for small equivalent widths the lower resolution FOS data yield equivalent widths systematically larger than values obtained from the GHRS intermediate-resolution data.

4.1. *Velocities*

The 3C 273 absorption-line data we have obtained have moderate signal-to-noise ratio and are adversely affected by the substantial amount of spectroscopic blurring because of the use of the large entrance aperture (see the spectroscopic spread function shown in Fig. 2). It therefore is difficult to study the details of the component structure of the absorption as revealed in the optical data summarized in § 3. The UV absorption-line profiles shown in Figure 2 have the following velocity characteristics: The weaker low ionization state absorption lines of Mn II, S II, and Si II, which trace the bulk of the neutral medium along the sight line, have average velocities of about -5 km s^{-1} and widths (FWHM) of approximately 60–100 km s^{-1}. These lines evidently are tracing the group of absorption components situated within ± 20 km s^{-1} seen in H I 21 cm emission, and Ca II and Na I absorption (see § 3). The strongest low-ionization lines extend to positive and negative velocities with full widths at half-intensity from ~ 120 (Fe II and Mg II) to ~ 150 km s^{-1} (Si II and C II). The rest equivalent widths for these lines expressed in velocity units reveal similar extents. The strong low ionization state lines appear to be tracing the higher velocity dispersion H I seen in the 21 cm emission line profile from Lockman & Savage (1993) shown at the top of Figure 2. Neutral hydrogen emission in that profile can be traced from approximately -60 to $+50$ km s^{-1}. The full velocity extent of the observed absorption-line profiles ranges from approximately -100 to $+100$ km s^{-1}. However, the broad wings on the spectroscopic spread function is smoothing the wings of the strongest absorption lines. Inspection of the original and deconvolved profiles for these same data presented by Brandt et al. (1993) allows an assessment of this problem. For the broadest and strongest lines the deconvolved profiles have overall extents approximately 10% less than the original profiles shown in Figure 2. However, the FWHM values of the deconvolved data are nearly the same as for the data of Figure 2.

The measurements show no evidence for high-velocity absorption in the lines of Mg II $\lambda\lambda$2796.352 and 2803.531, for the velocity range $|v_{\rm helio}|$ from 100 to 1000 km s^{-1} with a 3 σ detection limit of 0.05 Å. For Si II λ1260.422 and C II λ1334.532 the presence of absorption wings on the principal absorption profiles limits the search range for isolated high-velocity absorption to $v_{\rm helio}$ from $+140$ to $+1000$ km s^{-1} for Si II and from -140 to -1000 km s^{-1} for C II. For each of these ions the 3 σ detection limit is approximately 0.06 Å. Note that the absorption wings on the very strong lines are less apparent in the deconvolved spectra (see Brandt et al. 1993) and may not be real.

The high-ionization lines of N V, C IV, and Si IV are strong and broad with velocity extents comparable to that for the low-ionization absorption. In particular, the C IV $\lambda\lambda$1548.195 and 1550.770 lines have FWHM ~ 130 and 110 km s^{-1}, respectively. There are interesting similarities and differences between the profiles for the various high-ionization lines which are discussed further in § 4.3. The Si IV λ1393.755 line is contaminated by a Lyman-α forest line (see § 4.4).

High-velocity (100 km s^{-1} $< |v_{\rm helio}| <$ 1000 km s^{-1}) absorption by Si IV and C IV is not evident in the spectra with 3 σ upper limits for the equivalent widths of 0.05 Å for Si IV and 0.1 Å for C IV.

4.2. *Equivalent Widths*

Line equivalent widths and their errors are listed in Table 2. The errors include the statistical error and an estimate of the continuum placement error. The equivalent width for Si IV λ1393.755 includes a correction for intergalactic Lyman-α con-

tamination as discussed in § 4.4. The value for O I λ1302.169 is the observed value and is smaller than the actual value because of an unknown amount of Earth atmospheric O I emission. The equivalent widths in Table 2 differ slightly from those in Morris et al. (1991). Our equivalent widths are based on direct integration rather than on profile fitting, and our processed spectra have a more reliable background correction and incorporate more recent versions of the calibration files. The measured values of line strength based on the GHRS intermediate-resolution data are more accurate than results based on FOS data from Bahcall et al. (1991a) or based on the *IUE* measurements of Burks et al. (1991). Comparisons of GHRS and FOS equivalent widths are found in Brandt et al. (1993).

With the exception of the Si IV line profiles, the *IUE* data of Burks et al. (1991) are rather noisy and the equivalent widths have large errors. For example, we note that for the GHRS measurements the equivalent width of C IV λ1548.195 is less than that for C II λ1334.532, while for the *IUE* data the reverse is true. Because of large errors in the *IUE* measurements for a faint source like 3C 273, some of the comments about the relationship between high- and low-ionization absorption found in Burks et al. are invalid. However, the *IUE* data for Si IV agree well with the GHRS results. The elevated continuum due to the presence of Lyman-α emission from 3C 273 enhances the quality of the *IUE* and GHRS Si IV results. The *IUE* profile for Si IV λ1393.755 is particularly significant, since it reveals the contaminating intergalactic Lyman-α H I absorption at a resolution of 25 km s^{-1}, which is somewhat higher than the resolution of the LSA GHRS spectra (see § 4.4).

4.3. *Column Densities*

Many of the absorption lines we have recorded are so strong that they are only suitable for deriving lower limits to column density. Other lines may yield accurate column densities, but care is required to assess the level of saturation in the observed profiles properly. Our analysis uses and contrasts the standard curve-of-growth method and the apparent optical depth method (Savage & Sembach 1991).

A curve of growth for the weakly to moderately saturated low-ionization lines Si II λ1808.013, Ni II λ1370.132, Mn II λλ2576.977, 2594.499, 2606.462, Si II λλ1250.584, 1253.811, 1259.519, and C II* λ1335.703 is shown in Figure 3*a*. The solid curve represents the best-fit single-component Doppler-broadened curve of growth, which has a Doppler spread parameter $b = 2^{1/2}\,\sigma = 18.6$ km s^{-1}. The positions of the measurements in the plot imply very little line saturation for Si II, Ni II, Mn II, and C II*, but substantial saturation for S II. The true absorption toward 3C 273 exhibits multiple components spread over a velocity range from −25 to +25 km s^{-1}. The assumption that it is valid to fit the data to a single-component curve of growth is not particularly secure. The different species may have a different distribution from one absorbing cloud to the next. For example, Ni II, which is generally highly depleted from the gas phase, would be expected to behave differently from S II, which generally shows little or no depletion in neutral interstellar clouds.

The strong lines for such species as C II, Mg II, Si II, and Fe II mostly provide information about the higher velocity dispersion gas evident in the 21 cm emission profile of Figure 2. Requiring the weak low-ionization lines and the strong low-ionization lines to fit a single-component Doppler-broadened curve of growth yields a value of *b* for the best fit of 31.6 km s^{-1} which is substantially larger than that obtained from Figure 3*a* ($b = 18.6$ km s^{-1}). Using the larger value of *b* produces column densities for such species as S II which are smaller than those based on the curve of growth for the weak lines alone. This is because a simple single-component curve of growth is a poor approximation to an absorption composed of several components with modest values of *b* and high velocity dispersion components with substantially larger values of *b*. This particular problem has compromised most attempts to obtain reliable element abundances from QSO absorption-line data.

A curve of growth for the high-ionization lines of Si IV λλ1393.755, 1402.770, C IV λλ1548.195, 1550.770, and N V λλ1238.821, 1242.804 is shown in Figure 3*b*. The value of the equivalent width for Si IV λ1393.755 which is contaminated by

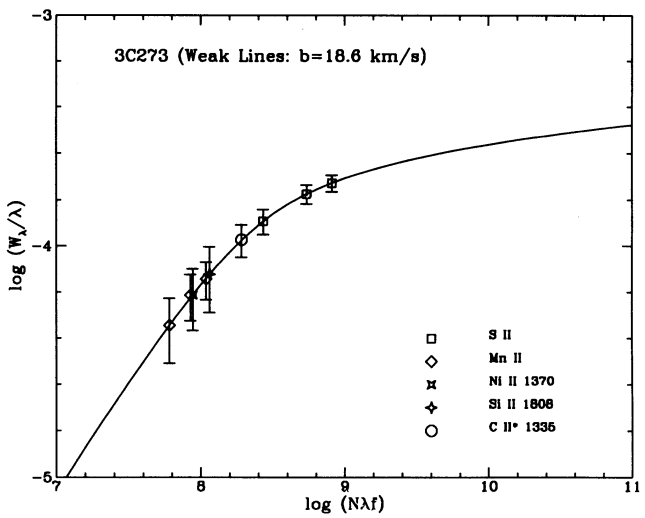

FIG. 3*a*

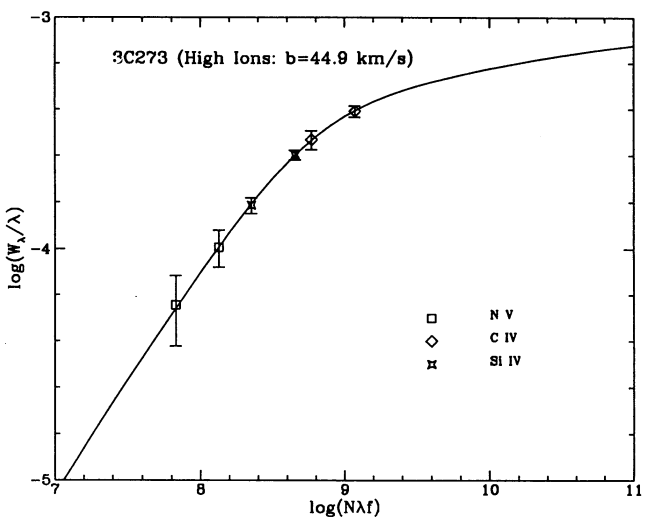

FIG. 3*b*

FIG. 3.—Values of log (W_λ/λ) from Table 2 plotted against log ($Nf\lambda$) and fitted to simple single-component Doppler-broadened curves of growth (*a*) for the weak low-ionization lines of S II, Si II, Mn II, C II*, and Ni II and (*b*) for the high-ionization lines of N V, C IV, and Si IV. The best-fit Doppler spread parameters are $b = 18.6$ km s^{-1} for the low ions and $b = 44.9$ km s^{-1} for the high ions.

intergalactic Lyman-α absorption, is the deblended equivalent width from Table 2 and § 4.4. Among the high-ionization lines, those for C IV are the most saturated and play a primary role in determining the value of the Doppler spread parameter that yields the best fit, $b = 44.9$ km s^{-1}. As in the case of the low-ionization species, we have forced the measurements for the three species to fit a simple curve of growth based on a single-component Doppler-broadened absorbing medium. The actual line profiles show differences from ion to ion, which suggests that this simple assumption is a crude approximation.

The low and high ionization state column densities obtained from this simple curve-of-growth analysis are listed in Table 3. The errors listed allow only for observational errors and not for the systematic errors that might occur because of the invalidity of the basic assumption that the data can be fitted to a single curve of growth defined by a one-component absorption. The importance of this systematic error will increase as the degree of saturation increases. Thus, for the low ions, we would expect the systematic errors to be largest for S II and C II*. For the high ions, the systematic errors will be largest for C IV.

The apparent optical depth method for the analysis of interstellar absorption-line data is described by Savage & Sembach (1991). Applications of the method to interstellar absorption-line data are found in Savage et al. (1989), Joseph & Jenkins (1991), and Sembach & Savage (1992). The method exploits all the information contained in complex absorption-line profiles and makes it possible to evaluate and in some cases correct for line saturation effects.

An application of the apparent optical depth method to the absorption produced by the highly ionized gas toward 3C 273 is illustrated in Figures 4 and 5. The apparent optical depth, $\tau_a(v)$, as a function of velocity of an absorption is given by

$$\tau_a(v) = \ln [I_c(v)/I_{\rm obs}(v)] , \quad (1)$$

where $I_c(v)$ is the estimated intensity in the continuum and $I_{\rm obs}(v)$ is the observed intensity in the absorption line as a function of velocity. The different measures of $\tau_a(v)$ are then converted into measures of apparent column density per unit velocity interval, $N_a(v)$ [atoms cm^{-2} (km s^{-1})$^{-1}$], through the relation

$$\log N_a(v) = \log \tau_a(v) - \log (f\lambda) + 14.576 , \quad (2)$$

where the wavelength λ is in angstroms. This expression follows from the relation between the true optical depth and the true column density per unit of velocity,

$$\tau(v) = \frac{\pi e^2}{m_e c^2} f\lambda N(v) . \quad (3)$$

A comparison of the different $N_a(v)$ profiles for lines differing in $f\lambda$ provides an empirical way of assessing the degree of line saturation present in the true line profile. If the derived run of $N_a(v)$ with v is the same for the two or more lines differing substantially in $f\lambda$, we can be reasonably sure that the derived $N_a(v)$ curves are a valid representation of the true $N(v)$, but simply blurred by the instrumental resolution. In other words, unresolved saturated structure, if present, would manifest itself as a difference in the $N_a(v)$ curves for lines with different values of $f\lambda$ (Savage & Sembach 1991).

Plots of the logarithm of the apparent optical depth, log $\tau_a(v)$, and the logarithm of the corresponding apparent column density, log $N_a(v)$, for the doublet lines of Si IV, C IV, and N V are illustrated in Figure 4. The error bars reflect the statistical and continuum placement uncertainties. The sizes of these error bars are large away from the center of the absorption where the value of $\tau_a(v)$ is small and difficult to measure.

In Figure 5 the log $N_a(v)$ profiles for each member of the three doublets are compared. Open and filled circles represent the weak and strong member results, respectively. The error bars have been suppressed but can be judged with reference to Figure 4. Over the velocity range where the profiles are reasonably well measured, the solid and dotted lines connect the data points. For Si IV the striking difference in appearance between the values of log $N_a(v)$ for the weak and strong lines is the

TABLE 3

COLUMN DENSITIES AND DEPLETIONS

ION	CURVE OF GROWTH[a] log N_{best}	-1σ	$+1\sigma$	APPARENT OPTICAL DEPTH[b] log N_{best}	-1σ	$+1\sigma$	LOGARITHMIC DEPLETION
C II	...	...	...	> 14.94	...	...	...
C II*	14.05	13.93	14.20	14.07:	13.99:	14.14:	...
C IV	14.60	14.48	14.76	14.61	14.56	14.65	...
N V	13.84	13.76	13.92	13.84	13.75	13.89	...
O I	...	...	...	> 14.96	...	...	...
Mg II	...	...	...	> 14.20	...	...	...
Si II	15.06	14.85	15.24	15.03	14.88	15.14	− 0.74
Si IV	13.80	13.75	13.85	13.78	13.74	13.81	...
S II	15.60	15.45	15.84	15.65:	15.58:	15.70:	+ 0.16
Mn II	13.08	13.00	13.16	13.08	12.93	13.19	− 0.67
Fe II	...	...	...	> 14.68	...	...	...
Ni II	13.69	13.50	13.84	13.66	13.50	13.77	− 0.81

[a] Column densities and errors for the low and high ions based on the curves of growth shown in Figs. 3*a* and 3*b*.

[b] Column densities and errors based on the apparent optical depth method of Savage & Sembach 1991. The results listed above are inferred from the apparent column densities and corrections listed for each absorption line in Table 4.

[c] Logarithmic depletions, log (X/H) − log $(X/H)_\odot$, are listed using the best values of column densities from the apparent optical depth method, using log N(H I) = 20.22 ± 0.08 based on the Lyman-α line of H I (§ 3). Solar abundances are taken from Anders & Grevesse 1989 with the values log $(X/H)_\odot$ + 12.0 = 7.55, 7.27, 5.53, and 6.25 for Si, S, Mn, and Ni, respectively.

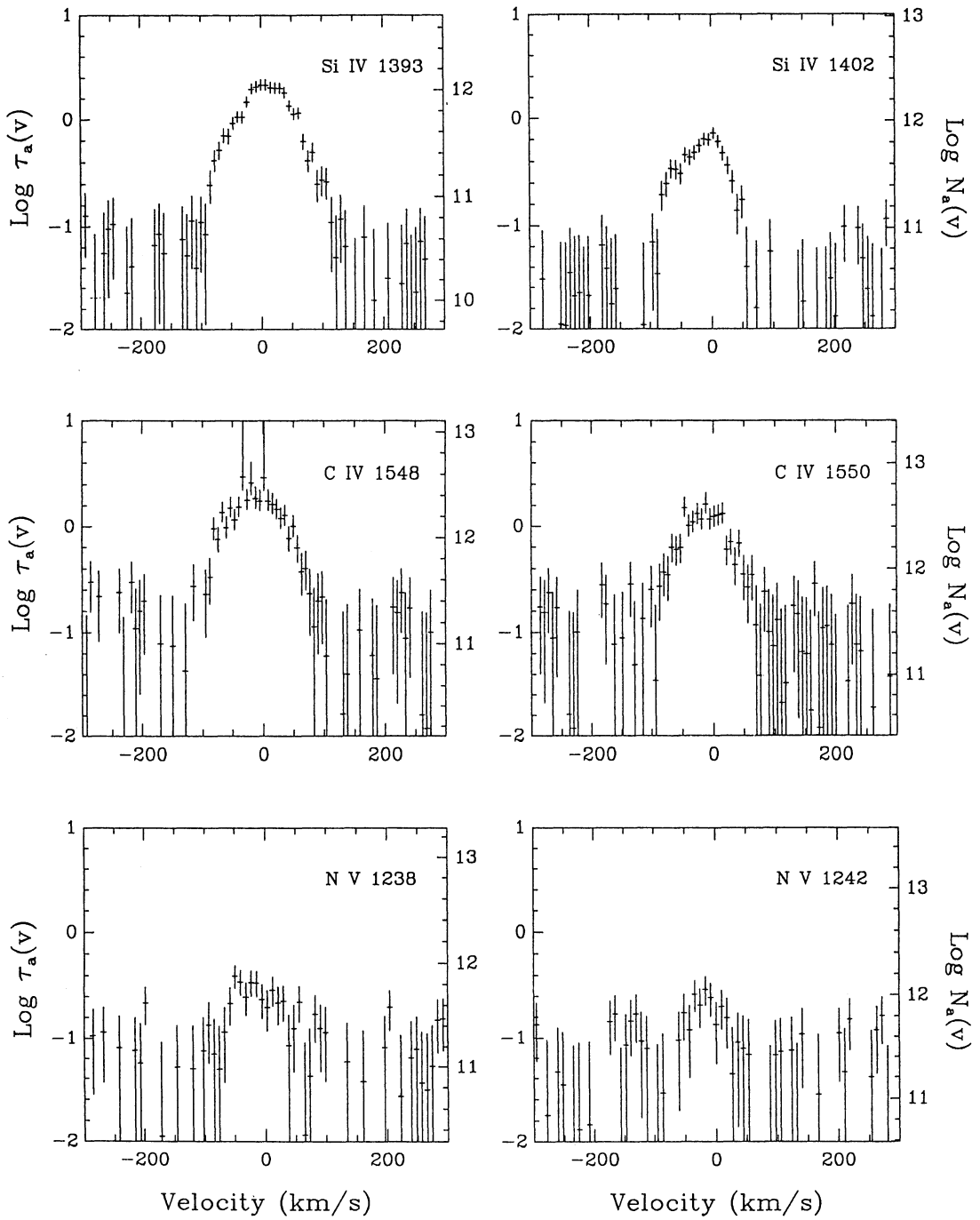

FIG. 4.—Logarithmic plots of apparent optical depth, $\tau_a(v)$, and apparent column density per unit velocity, $N_a(v)$ [atoms cm^{-2} (km s^{-1})$^{-1}$], for individual high-ionization doublet lines, plotted against heliocentric velocity (km s^{-1}). The error bars include the effects of statistical and continuum placement uncertainties. The curve for Si IV λ1393.755 is affected by a blended intergalactic Lyman-α line.

result of contamination of the Si IV λ1393.755 absorption by what is likely intergalactic H I Lyman-α absorption (see § 4.4). This contamination is severe for $v > -30$ km s^{-1}. For $v < -30$ km s^{-1} the weak-line and strong-line values of log $N_a(v)$ for Si IV agree well, which indicates that absorption over that velocity range does not contain unresolved saturation.

For C IV the weak- and strong-line values of log $N_a(v)$ agree well for -100 km s$^{-1} \leq v \leq -50$ km s^{-1} and for $+25$ km s$^{-1} \leq v \leq 75$ km s^{-1}. Near maximum absorption from -50 to $+25$ km s^{-1}, the weaker line values of log $N_a(v)$ lie $\sim$0.1 dex higher than the strong-line values, implying the onset of unresolved saturation in the core of the absorption.

For N V the weak-line values of log $N_a(v)$ lie higher than the strong-line results for the velocity range of maximum absorption. However, the errors for the two profiles are substantial, and the observed weakness of the absorption suggests that unresolved saturation should not be a problem.

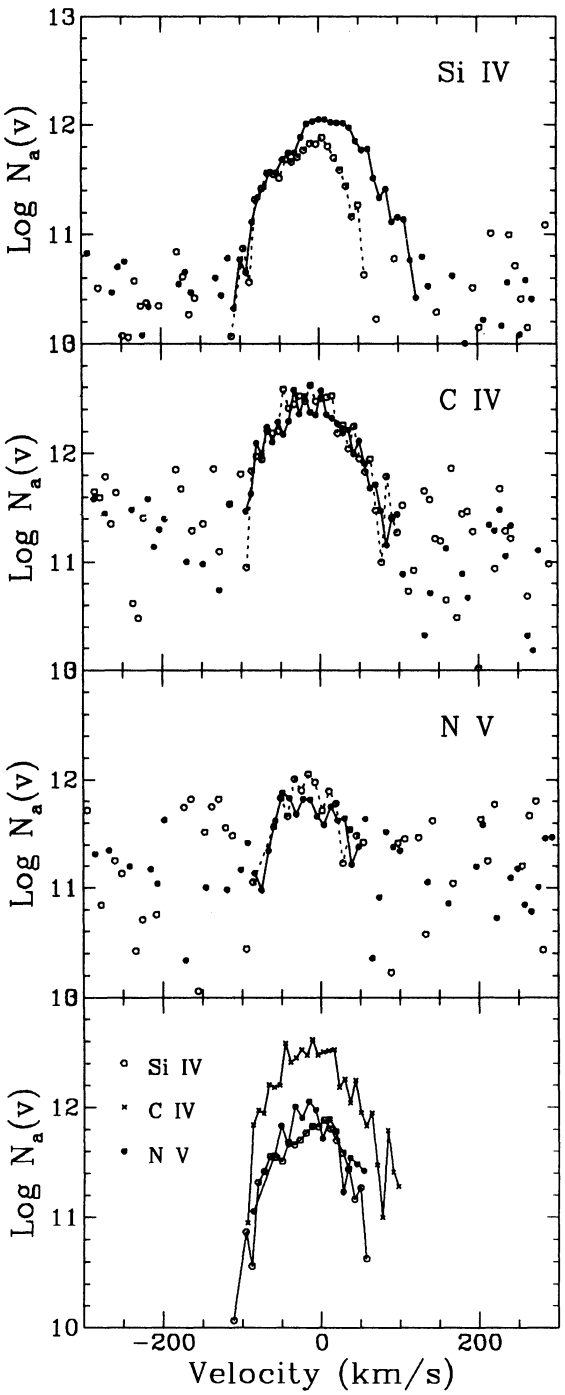

FIG. 5.—Logarithmic plots of apparent column density per unit velocity, $N_a(v)$ [atoms cm^{-2} (km s^{-1})$^{-1}$], vs. heliocentric velocity (km s^{-1}), for the individual high-ionization doublet lines from Fig. 4 are compared in the upper three panels. In each case the strong component of the doublet is represented with filled circles and the weak component with open circles. These data points are connected with solid or dashed lines where the absorption is reliably measured. The errors on each point can be judged with reference to Fig. 4. The curve for Si IV λ1393.755 is affected by a blended intergalactic Lyman-α line. In the lower panel the values of log $N_a(v)$ derived from the lines of Si IV λ1402.770, C IV λ1550.770, and N V λ1238.821 are intercompared. The log $N_a(v)$ profile for Si IV is more strongly peaked toward $v \sim 0$ km s^{-1} than that for C IV and N V.

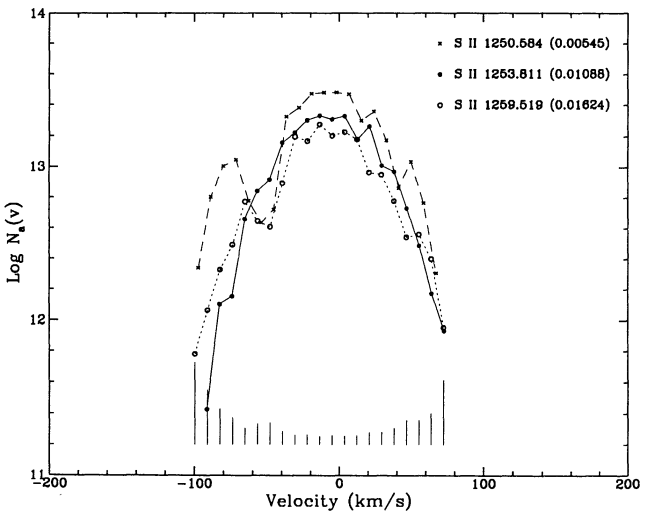

FIG. 6.—Logarithmic plots of apparent column density per unit velocity, $N_a(v)$ [atoms cm^{-2} (km s^{-1})$^{-1}$], vs. heliocentric velocity (km s^{-1}), for the individual lines S II $\lambda\lambda$1250.584 (*crosses*), 1253.811 (*filled circles*), and 1259.519 (*open circles*) are compared. The *f*-value for each line is indicated on the figure (in parentheses). The +1 σ errors appropriate for the S II λ1259.519 data points are shown at the bottom of the plot. The errors for the other S II lines are similar. Note that the values of log $N_a(v)$ near peak absorption lie highest for the S II λ1250.584 line which has the smallest *f*-value.

The lower panel of Figure 5 provides a comparison among the log $N_a(v)$ profiles for Si IV λ1402.770, C IV λ1550.770, and N V λ1238.821. There are differences in the profile shapes among the three high-ionization lines. For example, the Si IV profile is more strongly peaked near $v \sim 0$ km s^{-1} than the profiles for C IV or N V. *HST* observations along other sight lines through the halo have also revealed profile differences between the high-ionization lines of Si IV and C IV (see Spitzer & Fitzpatrick 1992).

Curves of log $N_a(v)$ for the S II $\lambda\lambda$1250.584, 1253.811, and 1259.519 triplet are shown in Figure 6. The 1 σ errors appropriate for S II λ1259.519 are shown at the bottom of the figure. The errors for the other S II lines are quite similar. This series of log $N_a(v)$ curves illustrates well the effects of unresolved saturation. Near maximum absorption, where the observational errors are small, the curves for the stronger lines at 1253.811 and 1259.519 Å lie $\sim$0.17 and $\sim$0.28 dex below the curve for λ1250.584. This amount of discrepancy for lines that differ in values of $f\lambda$ by factors of 2 and 3, respectively, indicates substantial saturation (Savage & Sembach 1991), implying that the true curve of log $N(v)$ will lie above that for the weak 1250.584 Å line by an amount given approximately by 0.24 dex (see Fig. 10 and Table 4 of Savage & Sembach 1991). Note that the curve of growth given in Figure 3*a* also indicates substantial saturation for the weakest S II line. There are substantial differences in the S II log $N_a(v)$ profiles in the velocity range from -40 to -100 km s^{-1}. The apparent enhancement in log $N_a(v)$ for S II λ1250.584 at approximately -75 km s^{-1} is not likely due to S II, since it does not appear in the curves for the other S II lines. This enhancement probably is a 3 σ noise excursion.

Logarithms of integrated apparent column densities for all the absorptions are given in Table 4, where $N_a = \int N_a(v)\,dv$. The velocity integration range is the same as for the equivalent widths (see Table 2). For weak absorption lines the value of log N_a will be a good measure of the actual value of log N. However, for the strong lines the values of log N_a will be

TABLE 4

APPARENT COLUMN DENSITY FOR INDIVIDUAL LINES

Ion	λ[a] (Å)	log N_a[b]	$-1\ \sigma$[c]	$+1\ \sigma$[c]	Δ log N[d]
C II	1334.532	> 14.94	...	...	...
C II*	1335.703	13.92	13.84	13.99	0.15:
C IV	1548.195	14.47	14.44	[e]	...
C IV	1550.770	14.54	14.49	14.58	0.07
N V	1238.821	13.82	13.74	13.90	0.00
N V	1242.804	13.86	13.69	13.98	0.00
O I	1302.169	14.96	14.93	14.98	...
Mg II ...	2796.352	> 13.93	...	...	...
Mg II ...	2803.531	> 14.20	...	...	...
Si II	1260.422	14.02	14.00	[e]	...
Si II	1304.370	14.56	14.54	14.59	...
Si II	1526.707	> 14.48	...	...	...
Si II	1808.013	14.99	14.84	15.10	0.04
Si IV	1393.755	[f]	...	...	...
Si IV	1402.770	13.78	13.74	13.81	0.00
S II	1250.584	15.41	15.34	15.46	0.24:
S II	1253.811	15.24	15.20	15.29	...
S II	1259.519	15.14	15.10	15.18	...
Mn II ...	2576.877	13.02	12.94	13.10	...
Mn II ...	2594.499	13.04	12.93	13.13	...
Mn II ...	2606.462	13.05	12.90	13.16	0.03
Fe II	2586.650	14.68	14.66	14.71	...
Fe II	2600.173	> 14.37	...	...	...
Ni II	1370.132	13.63	13.47	13.74	0.03

[a] Rest-frame, vacuum wavelength from Morton 1991.

[b] Best estimate of the integrated *apparent* column density from the $N_a(v)$ method.

[c] The 1 σ bounds of the estimated apparent column density.

[d] Correction to the apparent column density to account for unresolved saturation structure.

[e] The upper bound cannot be estimated because the flux level at the line center is less than 1 σ above zero, i.e., consistent with zero.

[f] No independent information is available from Si IV λ1393.755, since it is blended with another line.

smaller than the actual value of log N. This is evident when inspecting the results for the four lines of Si II where the weakest 1808.013 Å line gives the largest value of the integrated apparent column density, log $N_a = 14.99$.

For each ion with results listed in Table 4 we have reported final column densities based on the apparent optical depth method in Table 3. These are given either as lower limits to the value of log N or as actual measures of log N when weak-line measurements are available and it is possible to include corrections for modest amounts of unresolved saturation following the procedures of Savage & Sembach (1991). When corrections are applied, the value of that correction, Δ log N_a = log N − log N_a, is given in the last column of Table 4. In the case of the low-ionization species, the values of log N_a for the three lines of Mn II imply a small amount of saturation (0.03 dex) for the weak 2606.462 Å line, which is consistent with the curve of growth shown in Figure 3*a*. The lines of Si II λ1808.013 and Ni II λ1370.132 have maximum values of $\tau_a(v)$ similar to those for Mn II $\lambda\lambda$2594.499 and 2606.462, respectively, and also likely have the small saturation corrections listed. For S II the correction to λ1250.584 is estimated to be 0.24 dex based on the differences between log N_a for the three S II lines and the empirical correction scheme of Savage & Sembach (1991; see their Fig. 10 and Table 4). However, a correction this large implies substantial saturation, and the final result given in Table 3 for S II is listed as uncertain (denoted by the colons). The maximum apparent optical depth of C II* λ1335.703 implies a correction intermediate between that for S II λ1250.584 (0.24 dex) and Mn II λ2576.877 (0.06 dex). We have indicated an uncertain logarithmic mean correction of 0.15 dex.

For the high ions the correction to C IV λ1550.770 is estimated to be 0.07 dex, again following the empirical doublet correction scheme of Savage & Sembach (1991). The maximum apparent depths of the weaker lines of Si IV λ1402.770 and N V $\lambda\lambda$1238.821 and 1242.804 imply corrections that are substantially smaller than for C IV λ1550.770. Assuming these small corrections to scale linearly with the apparent maximum optical depth in the various high-ionization lines, we infer negligible corrections for these weaker lines.

An inspection of Table 3 reveals that the curve-of-growth method and the apparent optical depth method produce similar results. However, the apparent optical depth method provides better column density limits and also yields more detailed information about the actual velocity structure of the absorption (see Figs. 4–6). It was through a simple initial inspection of apparent optical depth profiles that the realization of the strong intergalactic contamination of the Si IV λ1393.755 absorption was made by Morris et al. (1991).

The scientific implications of the column densities given in Table 3 are discussed in § 5.

4.4. *Intergalactic Lyman-α Contamination of* Si II λ1393.755

Morris et al. (1991) noted that the apparent optical depth profiles and equivalent widths for the Si IV doublet lines are incompatible with the factor of 2 difference in the product $f\lambda$. This problem is clearly revealed in the log $N_a(v)$ profiles for Si IV shown in Figure 5. The stronger line Si IV λ1393.755 exhibits extra absorption over the velocity range from approximately −30 to +130 km s^{-1}. That extra absorption is probably due to a contaminating intergalactic H I Lyman-α line. Figure 7 illustrates the result of deblending the contaminating

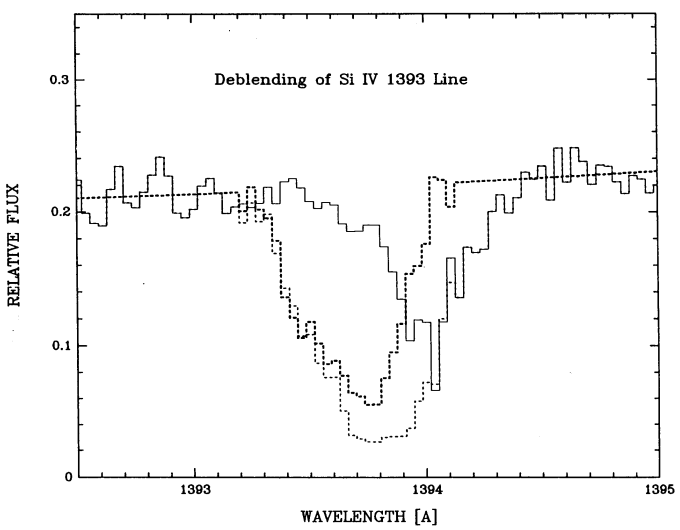

FIG. 7.—Three curves illustrating the observed Si IV λ1393.755 line profile (*light dashed line*), the inferred Si IV absorption attributed to the Milky Way (*heavy dashed line*), and the contaminating Lyman-α line (*solid line*).

line by computing the velocity-dependent Si IV apparent optical depth, $\tau_{1402}(v)$, from the weaker line Si IV λ1402.770. The true Si IV λ1393.755 absorption was assumed to have a shape and strength given by exp $[-2\tau_{1402}(v)]$. The difference between these two absorptions produces a residual absorption centered at 1402.02 Å or +56 km s^{-1} with respect to the Si IV line, which we attribute to intergalactic H I Lyman-α. The equivalent widths of the two deblended absorptions are W_λ = 0.356 Å for Si IV λ1393.755 and W_λ = 0.216 Å for the contaminating Lyman-α line. The deblending reported here is consistent with the Si IV profile shown in Figure 2 of Burks et al. (1991), which clearly reveals an extra velocity component near $v_{\rm helio} \sim 44$ km s^{-1}, which is displaced from the center of Si IV λ1393.755 by about 52 km s^{-1}.

We find no evidence in our data set for other intergalactic absorption lines contaminating Milky Way lines. A possible exception is the weak feature near −75 km s^{-1} in the S II λ1250.584 profile. However, that feature has low statistical significance (see error bars in Fig. 6). Morris et al. (1991) observed 10 candidate intergalactic Lyman-α lines toward 3C 273 between 1235 and 1406 Å with W_λ exceeding 50 mÅ, implying a low-redshift intergalactic line density of 0.058 lines Å^{-1}. The same wavelength region contains 14 Milky Way lines. Thus, the expected number of cases where an intergalactic line is within ±0.5 Å of a Milky Way line is approximately 0.058 × 14 = 0.82. Therefore, it is not too surprising that we indeed found one example of a blend.

5. DISCUSSION

The sight line to 3C 273 traces neutral, weakly ionized, and highly ionized regions of Galactic disk and halo gas. In the following discussions we first consider the abundance and physical condition information about the neutral and weakly ionized gas (§ 5.1) and the highly ionized gas (§ 5.2). We discuss the kinematics of the gas in § 5.3 and compare the results for the sight line to 3C 273 with measurements for other sight lines through the Milky Way to extragalactic objects in § 5.4. Our discussion ends with § 5.5, where we compare the Galactic disk and halo absorption seen toward 3C 273 with that found in high-redshift damped Lyman-α systems.

5.1. *Neutral and Weakly Ionized Gas*

The interstellar medium of the Galaxy consists of different phases with different scale heights, velocity dispersions, temperatures, and ionization conditions. The neutral cloudy medium has a small scale height (~120 pc) and a small velocity dispersion (~10 km s^{-1}). A more turbulent phase of the neutral medium with a velocity dispersion of about 30 km s^{-1} has a more extended distribution away from the Galactic plane with a scale height of perhaps 500 pc (for a review see Dickey & Lockman 1990).

The lines of S II, Mn II, Ni II, and Si II for which we are able to obtain estimates of total column density probably mostly trace gas in neutral hydrogen regions. This is because these species have first ionization potentials of 23.4, 15.6, 18.2, and 16.3 eV, for S II, Mn II, Ni II, and Si II, respectively, we may encounter situations where these species also trace warm ionized gas. In comparing measures of H I and electrons toward high-latitude pulsars in globular clusters based on H I 21 cm emission and pulsar dispersion measures, Reynolds (1991) has found that N(H II)/N(H I) ranges from 0.23 to 0.63, with a median value of 0.34.

In the last column of Table 3 we have derived average logarithmic depletions for S, Mn, Ni, and Si with the assumption that the observed lines of S II, Mn II, Ni II, and Si II are mostly produced in the neutral medium toward 3C 273. The depletion for species X is

$$\log [N(\mathrm{X})/N(\mathrm{H\ I})] - \log [N(\mathrm{X})/N(\mathrm{H\ I})]_\odot ,$$

where $\log [N(\mathrm{X})/N(\mathrm{H\ I})]_\odot$ is the solar abundance ratio, which is taken from Anders & Grevesse (1989). The H I column density, $\log N(\mathrm{H\ I}) = 20.22 \pm 0.08$, is from the profile fitting to the FOS Lyman-α data (§ 3). The resulting logarithmic depletions for S, Mn, Si, and Ni are +0.16:, −0.67, −0.74 and −0.81, respectively. The formal value for S, which comes from S II, suggests an overabundance of 45%. However, among the four elements we have analyzed, the column density for S II is the least reliable because of the sizable saturation correction. If the formal result is correct, the 45% overabundance may be due to the ionized gas phase discussed above.

Ignoring the ionization problem, the depletions for Mn, Si, and Ni imply that these elements are underabundant in the gas phase by factors of ~5, presumably due to the presence of these elements in interstellar dust. In diffuse clouds of moderate density Mn, Si, and Ni are normally quite highly depleted (−1.2 to −2,2 dex; for a review see Jenkins 1987). The modest depletion for the sight line to 3C 273 appears compatible with the empirical result that regions with lower average sight-line density have modest depletions. With a total H I column density of 1.66×10^{20} atoms cm^{-2} we estimate an average sight-line hydrogen density of 0.05 atoms cm^{-3} if the H I extends over approximately two scale heights or 1000 pc. For such a mean sight-line density the results of Table 3 are quite compatible with the empirical trends reviewed by Jenkins (1987). The first 1000 pc of the sight line to 3C 273 evidently samples neutral hydrogen associated with the lower density neutral medium found between diffuse clouds.

The ground state of the C II ion is split into two fine-structure levels. In the diffuse interstellar medium C II is excited by collisions with electrons and hydrogen atoms. Emission from the excited level produces radiation at 157.7 μm which is believed to be the primary cooling mechanism for gas in the cool neutral and warm ionized medium (Kulkarni & Heiles 1987). Therefore, our measurement of the column density of atoms in the excited state, $\log N(\mathrm{C\ II^*}) = 14.07$, allows us to estimate the cooling rate of the gas in the galaxy toward 3C 273 per hydrogen atom

$$l_c = h\nu_{12} N(\mathrm{C\ II^*}) A_{21}/N(\mathrm{H\ I}) .$$

With an Einstein A-value $A_{21} = 2.36 \times 10^{-6}$ s^{-1}, N(C II*) $= 1.17 \times 10^{14}$ cm^{-2}, and N(H I) $= 1.66 \times 10^{20}$ cm^{-2}, we obtain a cooling rate per hydrogen

$$l_c = 2.1 \times 10^{-26} \text{ ergs s}^{-1} \text{ hydrogen}^{-1} .$$

This value is approximately 5 times smaller than the average value found by Pottasch, Wesselius, & van Duinen (1979) for eight different lines of sight through disk gas. If, instead of comparing the cooling rate with N(H I), we correct for the presence of ionized gas by adopting the procedure of Pottasch et al. (1979) and compare the cooling rate with $N(\mathrm{H\ I} + \mathrm{H^+}) = N(\mathrm{S\ II})\,[N(\mathrm{H})/N(\mathrm{S})]_\odot$, which is 45% larger than the value of N(H I), we obtain from the S II column density in Table 3 the cooling rate per nucleon,

$$l_c = 1.4 \times 10^{-26} \text{ ergs s}^{-1} \text{ nucleon}^{-1} .$$

Kulkarni & Heiles (1987) show that for a given cosmic-ray ionization rate, ζ_{cr}, the cooling rate is proportional to pressure. For the average cooling rate observed by Pottasch et al. (1979), $l_c \sim 10^{-25}$ ergs s^{-1} nucleon^{-1}, they estimate $P/k = 8000$ cm^{-3} K for a cosmic-ray ionization rate assumed to be 10^{-16} s^{-1}. The data for 3C 273 imply an average pressure of about 1100 cm^{-3} K if the temperatures of the absorbing clouds and the cosmic-ray ionization rates are similar in disk and low halo clouds.

5.2. *Highly Ionized Gas*

The sight line to 3C 273 through Galactic disk and halo gas is extremely important because measurements now exist for a wide range of highly ionized species, including Si IV, C IV, N V, and O VI. The radiative production of these ions requires photons with energy exceeding 33, 47, 77 and 113 eV, respectively. Under conditions of equilibrium coronal ionization the four ions peak in abundance at temperatures of approximately 0.8×10^5, 1×10^5, 2×10^5, and 3×10^5 K, respectively (Shapiro & Moore 1976). N V and O VI are particularly important as tracers of hot interstellar gas because it is very difficult to produce these two ions with radiation from hot stars given the expected presence of a strong He^+ absorption edge at 54 eV in normal stellar energy distributions for hot stars. Thus, the presence of N V and O VI absorption is often taken to be the signature of interstellar gas with temperatures near $(2–3) \times 10^5$ K.

In Table 5 we have compared theoretical and observational values of column densities for Si IV, C IV, N V, and O VI in Galactic disk and halo gas. In columns (2) and (3) the column density predictions of photoionized halo models and cooling fountain models are listed. In each case the expected column density perpendicular to the Galactic plane to one side of the Galaxy, $N(\text{ion})|\sin b|$, is given. The notes to the table provide information about the parameters used in the modeling. In column (4) we give average results from Sembach & Savage (1992) based on high-quality measures of Si IV, C IV, and N V toward 10 halo stars with $|z| < 3$ kpc. In columns (5) and (6) we list results for $N(\text{ion})|\sin b|$ for the path to the SMC and the LMC from Fitzpatrick & Savage (1983) and Savage et al. (1989). Column (7) lists the 3C 273 results for $N(\text{ion})|\sin b|$ from this paper, along with a lower limit for $N(\text{O VI})|\sin b|$ obtained from the *Astro 1* observations of O VI absorption by Davidsen et al. (1992).

The values of $N(\text{ion})|\sin b|$ for the high ions toward 3C 273 are about 2–4 times larger than the same ions toward the SMC and the LMC and about twice as large as for a large group of measurements to halo stars with $|z|$ typically less than 3 kpc. Some of the enhancement in the abundance of these species toward 3C 273 may be due to contributions to the absorption from hot gas associated with those energetic events that created radio loops I and IV. However, we cannot rule out the possibility that enhanced absorption toward 3C 273 is simply due to the patchy nature of the distribution of highly ionized gas in the halo. For example, near $|z| \sim 1$ kpc, Sembach & Savage (1992) see a peak-to-peak spread of a factor of 10 in values of $N(\text{C IV})|\sin b|$.

The observed ionic ratios for the sight line to 3C 273 are $N(\text{C IV})/N(\text{Si IV}) = 6.8^{+2.3}_{-1.2}$ and $N(\text{C IV})/N(\text{N V}) = 5.9^{+2.0}_{-1.2}$. For stars in the low halo ($|z| < 3$ kpc), Sembach & Savage (1992) have found average ratios of $N(\text{C IV})/N(\text{Si IV}) = 3.6 \pm 1.3$ and $N(\text{C IV})/N(\text{N V}) = 4.6 \pm 2.7$. The larger value of $N(\text{C IV})/N(\text{Si IV})$ toward 3C 273 compared with sight lines into the low halo may imply changing ionization conditions with $|z|$ or a substantial enhancement of the column density of C IV toward 3C 273, perhaps as a result of the events that created radio loops I and IV.

The theory for the origin of highly ionized gas at large distances from the Galactic plane has been recently reviewed by Spitzer (1990). In Table 5 we compare the observations with the predictions of two very different types of models. In column (2) we list the predicted column densities for the cosmic-ray–supported photoionized halo calculations of Hartquist, Pettini, & Tallant (1984). The comparison immediately reveals that the principal problem of such models is their inability to produce the observed amounts of N V and O VI. For the particular

TABLE 5

COLUMN DENSITIES FOR HIGHLY IONIZED MILKY WAY HALO GAS

Ion (1)	Photoionized Halo[a] $N\|\sin b\|$ (2)	Cooling Fountain[b] $N\|\sin b\|$ (3)	Milky Way Halo Stars[c] $N\|\sin b\|$ (4)	SMC HD 5980[d] $N\|\sin b\|$ (5)	LMC Sn 1987A[e] $N\|\sin b\|$ (6)	3C 273[f] $N\|\sin b\|$ (7)
Si IV	1.3×10^{14}	$(3.3–6.4) \times 10^{12}$	$\sim 3.5 \times 10^{13}$	2.8×10^{13}	1.9×10^{13}	5.4×10^{13}
C IV	1.2×10^{14}	$(4.3–7.9) \times 10^{13}$	$\sim 1.6 \times 10^{14}$	1.8×10^{14}	7.7×10^{13}	3.7×10^{14}
N V	7.3×10^{11}	$(2.8–3.6) \times 10^{13}$	$\sim 2.5 \times 10^{13}$	2.2×10^{13}	...	6.2×10^{13}
O VI	1.4×10^{11}	$(5.8–6.0) \times 10^{14}$	$> 3.0 \times 10^{13}$	...	...	$> 2.5 \times 10^{14}$

[a] Predicted column densities of highly ionized gas through the halo ($N|\sin b|$) based on the cosmic-ray–supported photoionized halo calculations of Hartquist, Pettini, & Tallant 1984. The model values listed are for the model in which warm (10^4 K) gas has a large filling factor and a large pressure scale height with $n_0 = 3 \times 10^{-3}$ cm^{-3} and $H = 3$ kpc. Note that these photoionized halo models produce very little N V and O VI.

[b] Predicted column densities of highly ionized gas through the halo ($N|\sin b|$) on one side of the Galaxy based on the time-dependent ionization calculations of Edgar & Chevalier 1986. The values assume a fountain mass flow rate of 4 $M_\odot$ yr^{-1} on each side of the Galactic plane. The two values of $N|\sin b|$ listed for each ion involve different assumptions about the sizes of the cooling regions.

[c] Values for Si IV, C IV, and N V are from Sembach & Savage 1992 for halo stars with $|z| < 3$ kpc. The value for O VI is from Jenkins 1978. The latter is listed as a lower limit because the sight lines only extend to $|z| \sim 1$ kpc.

[d] The values listed are for the sight line toward HD 5980 in the SMC, from Fitzpatrick & Savage 1983, and refer to gas with $v < 100$ km s^{-1}.

[e] The values listed are for the sight line toward SN 1987A in the LMC, from Savage et al. 1989, and refer to gas with $v < 120$ km s^{-1}.

[f] The value for O VI is from Davidsen et al. 1992. The rest are from this study.

model listed, the shortfall is about a factor of 10^2 for N v and more than a factor of 10^3 for O vi. In contrast, the cooling fountain model of Edgar & Chevalier (1986) produces an adequate amount of C iv, N v, and O vi but underproduces Si iv. However, the recent work of Shapiro & Benjamin (1991) has shown that the inclusion of self-ionizing radiation from the cooling flow can substantially enhance the amount of Si iv produced. It therefore appears that fountain flows with mass flow rates within a factor of 2 or 3 of about 4 $M_\odot$ yr^{-1} to each side of the Galactic plane are able to explain the data. In the case of the 3C 273 column densities a flow rate of about 12 $M_\odot$ yr^{-1} produces C iv and N v column densities within 50% of the measurements.

5.3. *Kinematics of the Gas*

With $v_{\rm LSR} = v_{\rm helio} + 2.3$ km s^{-1}, the average absorption-line heliocentric velocities listed in Table 2 indicate that the high ions have average LSR velocities of -14 (Si iv), -7 (C iv) and -14 (N v). These can be compared with -7 (Si ii λ1808), -6 (S ii), -2 (Mn ii) and -3 (Ni ii). In making this comparison we have purposely chosen the low-ionization lines with little or modest saturation, to compare with the high-ionization lines which also have modest saturation. In this comparison, the velocity difference between N v and S ii is the most significant, since these measurements were obtained with the same grating setup position and should have relative velocity errors much smaller than the typical absolute velocity error of 10 km s^{-1}. Evidently, in the direction of 3C 273 the highly ionized gas shows slightly greater inflow speeds than the neutral gas tracers.

Spitzer & Fitzpatrick (1992) noted possible differences in the Si iv and C iv absorption-line profiles for the sight line to the halo star HD 93521 and suggested that the result may be qualitatively consistent with the expectations for the return to the disk of cooling fountain gas. We also see substantial differences in the high-ionization profiles (see the lower panel of Fig. 5) that might be similarly interpreted. However, given the complexity of the profiles which exhibit differences at both negative and positive velocities, it appears that kinematical data for a number of sight lines will be needed before it will be possible to draw general conclusions. Along any given sight line, confusion will be introduced if the absorption is produced by gas having different origins (i.e., cooling hot fountain gas versus photoionized warm disk gas).

The strongest lines of such neutral gas tracers as C ii, Si ii, Mg ii, and Fe ii have full velocity extents at half-absorption strength ranging from $\sim$120 km s^{-1} (Fe ii and Mg ii) to $\sim$150 km s^{-1} (Si ii and C ii). These lines are probing the high velocity dispersion gas evident in the H i 21 cm emission-line profile from Lockman & Savage (1993) shown in Figure 2. That gas may be associated with the high velocity dispersion H i studied by Kulkarni & Fitch (1985). That phase of the H i is likely the phase that has a large scale height (Lockman & Gehman 1991).

The extension of the very strong absorption lines to negative and positive velocities is interesting. In the direction to 3C 273 the effects of Galactic rotation are expected to be small. If gas at very large distances from the plane corotates with gas in the underlying disk, the expected radial velocity of gas in the halo toward 3C 273 decreases from 0 to -6 km s^{-1} over a sight-line distance of 7 kpc and then increases back to 0 km s^{-1} over the next 7 kpc. However if at some large distance away from the plane there is a decoupling of the rotational motion of disk and halo gas, we might expect to begin to see evidence for that decoupling even for relatively high-latitude sight lines. For example, if at very large z distances in the direction to 3C 273 the gas rotational motions lag behind those in the disk by $\Delta\theta = \theta(z) - \theta_\odot$ km s^{-1}, that would show up as a radial velocity component,

$$v_r = \Delta\theta \sin l \cos b = \Delta\theta \sin 290^\circ \cos 64^\circ = -0.41\Delta\theta\ .$$

Therefore, if the gas at large z did not participate in Galactic rotation, we would have $\Delta\theta = -\theta_\odot = -220$ km s^{-1} (the rotational speed of the LSR) and $v_r = +90$ km s^{-1}. In this situation we would expect the observed profiles to exhibit a pronounced extension to large positive velocities. While some of the profiles show weak asymmetries on the positive velocity wings, the absence of a pronounced effect can be used to constrain models for the breakdown of corotation. However, compensating motions may occur as the result of flows of the gas in directions toward or away from the Galactic plane.

The strong low- or high-ionization lines show no evidence for absorption that might be associated with high-velocity clouds over the velocity range 100 km s^{-1} $< |v| <$ 1000 km s^{-1}. In particular, there is no evidence for absorption near the velocities $v_{\rm helio} = +213$ and $+261$ km s^{-1}, where Meyer & Roth (1991) found Ca ii absorption in the spectrum of SN 1991T, which lies 1°.4 from 3C 273. This result implies that the high-velocity gas in this direction has small-scale structure. Thin shells of gas associated with radio loops I and IV might explain this result. In the case of the feature Meyer & Roth (1991) saw at -89 km s^{-1} toward the supernova, it is possible that we are seeing the same gas toward 3C 273 in the wing of C ii λ1334.532.

5.4. *A Comparison with Other Extragalactic Sight Lines*

Most spectral observations of extragalactic sources with *HST* will need to allow for the strong foreground absorption produced by gas in the disk and halo of the Milky Way. The strength of that absorption will depend on the sight line as discussed by Savage (1988). Far-UV measurements through the entire halo have been reported for 3C 273 (this paper; Morris et al. 1991; Burks et al. 1991; Bahcall et al. 1991a), the LMC (Savage & de Boer 1981) and the SMC (Fitzpatrick & Savage 1983), and H1821+643 (Bahcall et al. 1992). To provide some insight into the range of variation to be expected, we illustrate in Figures 8*a* and 8*b* a comparison of the GHRS results for 3C 273 with the results for these other sight lines. In Figure 8*a* equivalent widths in angstroms are compared, while in Figure 8*b* equivalent widths in the more physically meaningful units of velocity ($W_v = W_\lambda c/\lambda$) are compared. For the LMC and SMC data, all absorption with $v < 150$ and $v < 100$ km s^{-1}, respectively, is assumed to be due to the Milky Way. In Figures 8*a* and 8*b* the filled circles are for HD 36402 in the LMC. The open circles are for HD 5980 in the SMC, and the open squares are for H1821+643. High-ionization lines are identified with the plus symbol. It is evident that the 3C 273 low-ionization absorption-line equivalent widths are intermediate in strength compared with the Milky Way absorption toward the SMC, the LMC, and H1821+643. The strongest low-ionization absorption lines toward extragalactic objects have a large variation of velocity width from $W_v \sim 70$ km s^{-1} (SMC) to 220 km s^{-1} (LMC and H1821+643). The intermediate case is 3C 273 ($W_v \sim 150$ km s^{-1}). It is interesting that the high-ionization lines exhibit less of a spread from sight line to sight line than the low-ionization lines. The high-ionization absorption is typically less saturated than the low-ionization

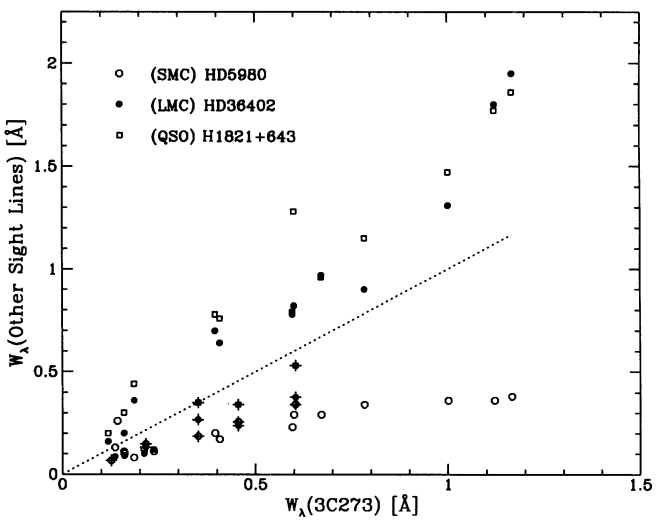

FIG. 8a

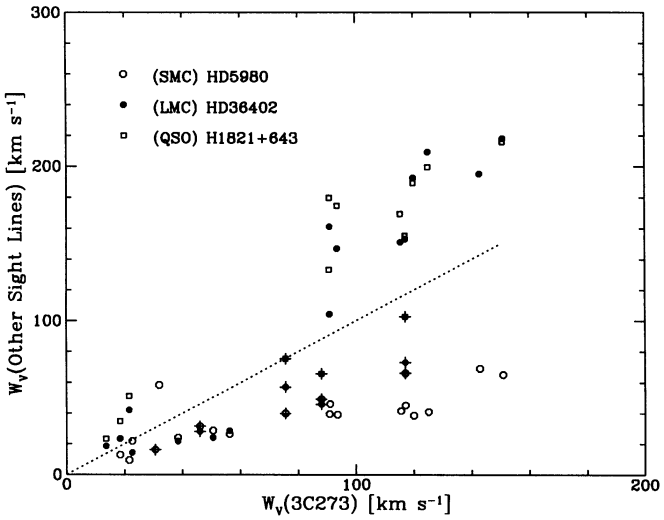

FIG. 8b

FIG. 8.—Equivalent widths in wavelength units, W_λ (Å), and velocity units, W_v (km s^{-1}) = $W_\lambda c/\lambda$, are compared for the sight line 3C 273 with values for the extragalactic sight lines to HD 5980 in the SMC (*open circles*), HD 36402 in the LMC (*filled circles*) and H1821 + 643 (*open squares*). Data for the high-ionization lines of Si IV, C IV, and N V are indicated with plus signs. (*a*) Plots of W_λ(other sight line) vs. W_λ(3C 273). (*b*) Plots of W_v(other sight line) vs. W_v(3C 273).

absorption. Therefore, the equivalent widths of the high-ionization absorption lines are mostly a measure of column density, while the equivalent widths of the low-ionization absorption lines are a measure of the breadth of a saturated absorption which is mostly influenced by the gas kinematics along the line of sight.

5.5. *A Comparison with QSO Absorption-Line Measurements*

The narrow metal absorption lines observed in spectra of high-redshift QSOs at redshifts $z_{abs} \ll z_{em}$ have generally been interpreted as arising from material in the disks and halos of intervening galaxies which happen to lie along the lines of sight (Bahcall & Spitzer 1969; Bergeron & Boisse 1991). Thus a direct comparison of these metal absorption systems at high redshifts with those seen at zero redshifts, such as UV absorption lines seen through the disk and halo of our Galaxy, should be very instructive. These types of comparisons have been scarce in the literature because good-quality data along lines of sight probing the entire Galactic halo have been difficult to obtain with the *IUE* satellite. Savage & Jeske (1981) have compared the UV absorption-line properties seen along the lines of sight toward the stars HD 36402 in the LMC and HD 5980 in the SMC with a sample of selected QSO absorption systems showing both low- and high-ionization species (the so-called mixed ionization systems; cf. Bergeron 1988), and found that the two types of absorption systems are remarkably similar in terms of ion species seen, equivalent widths, column densities, and velocity structures. Yet comparisons between Galactic halo absorption with QSO absorption systems selected on the basis of the C IV $\lambda\lambda$1548, 1550 doublet, which dominates the population of QSO metal-line systems, reveal a very different picture, in that Galactic absorption is dominated by low-ionization absorption, while C IV–selected QSO systems are characterized by stronger high-ionization absorption than low-ionization (Wolfe 1983; Danly, Blades, & Norman 1988). However, it must be pointed out that while the Galactic sight lines used for the comparisons by Wolfe (1983) and Danly et al. (1988) pass through the disk of the Galaxy, as well as the Galactic halo, most C IV systems probably only sample the extended halos surrounding high-redshift galaxies. There are also criticisms for using the LMC and the SMC sight lines for the comparison, since it is not universally agreed upon which absorption arises from halo material of our Galaxy and which absorption arises from material associated with the Magellanic Clouds (Savage 1988; York 1988). Given the controversial situation, and given the high-quality data on the 3C 273 sight line, which samples the entire Galactic halo to one side of the Galaxy, a comparison of the UV absorption-line properties along the 3C 273 sight line with representative QSO absorption systems is very meaningful. It may be argued that the 3C 273 sight line is not representative of Galactic halo absorption, since it penetrates through the radio loops I and IV. However, it may be precisely such structures as radio loops I and IV that give rise to the QSO metal absorption systems at high redshifts.

In order not to bias the comparison, it is necessary to compare the 3C 273 sight line with QSO metal systems with similar H I column densities. The systems suitable for this purpose are the damped Lyman-α systems. The damped systems have H I column densities in the range 1×10^{20} to 6×10^{21} atoms cm^{-2} and are believed to be produced when the QSO lines of sight penetrate through the disks and halos of high-redshift galaxies (Wolfe et al. 1986; Wolfe 1988). The damped systems always exhibit absorption of low-ionization species which are usually strong. They also often show detectable absorption due to highly ionized species, such as Si IV and C IV, which are usually somewhat weaker than the low-ionization absorption (Wolfe 1988; Lanzetta 1988; Turnshek et al. 1989; Lu 1991). Similar species are seen in Galactic disk and halo absorption. Very highly ionized species, such as O VI, are usually difficult to identify in QSO spectra, because the only O VI lines in the UV at 1031.93 and 1037.62 Å reside in the Lyman-α forest, where confusion noise from forest absorption lines are strong. Recently, however, Lu & Savage (1993) have detected O VI $\lambda\lambda$1031.93, 1037.62 doublet absorption in a composite QSO spectrum formed from a large number of C IV–selected systems. Most C IV systems are believed to arise from extended halo regions surrounding high-redshift galaxies.

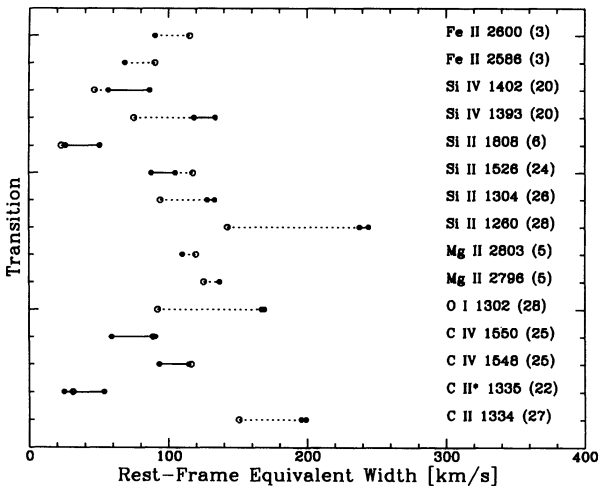

FIG. 9.—Milky Way absorption-line equivalent widths expressed in velocity units, W_v (km s^{-1}) = $W_\lambda c/\lambda$, for the 3C 273 sight line (*open circles*) are compared with the range of average results for QSO damped Lyman-α line systems (*filled circles connected with solid lines*). When the values do not overlap, the symbols are connected with a dashed line. The different species are indicated on the plot. The number in parentheses next to the rest wavelength of the absorption represents the number of damped Lyman-α systems included in the averaging. The O I measurement for the Milky Way is a lower limit because of contamination by terrestrial O I emission.

There are too few damped Lyman-α systems in the sample of Lu & Savage to determine reliably whether the damped systems also show O VI absorption. However, if damped Lyman-α systems indeed arise from disk gas of high-redshift galaxies, then the lines of sight should also pass through the halo surrounding the disks. Thus the damped systems should also show O VI absorption. The mean O VI column density estimated by Lu & Savage for the C IV systems is N(O VI) > 3.8 × 10^{14} atoms cm^{-2}, which is very similar to that along the 3C 273 sight line reported by Davidsen et al. (1992) (see Table 5).

In Figure 9 we plot the rest-frame equivalent widths of the strong UV absorption lines of both low and high ions toward 3C 273 in velocity units with those of the damped Lyman-α systems. The open circles represent the 3C 273 sight line. The data on the damped Lyman-α systems are obtained from literature for the damped systems compiled by Lu (1991).[2]

The systems in the sample have an average H I column density of $\langle N(\text{H I})\rangle$ = 1.2 × 10^{21} cm^{-2} and an average redshift of $\langle z\rangle$ = 2.4. Thus, the neutral hydrogen column density found in the average damped Lyman-α system of our sample is approximately 7 times greater than the neutral hydrogen column density (1.66 × 10^{20} cm^{-2}) produced by Milky Way disk gas toward 3C 273. While this difference would cause difficulties with relative abundance studies, our comparison of the equivalent widths of strongly saturated absorption lines mostly provides information about the kinematics or turbulence in the gas and not information about elemental abundances. For example, for the 3C 273 data, the equivalent widths for the strongly saturated lines of C II λ1334.53, Si II λλ1260.42, 1304.37, 1526.71, Fe II λλ2600.17, 2586.65, and Mg II λλ2796.35, 2803.53 are not determined by the column density of disk gas with low velocity dispersion. These equivalent widths are mostly established by the kinematical conditions in the low column density high velocity dispersion gas situated in the low halo of the Milky Way.

Sometimes the region of an expected absorption line is observed, but with no detection only an upper limit for the line equivalent width is reported. We have calculated the average equivalent width of each line in Figure 9 observed in damped Lyman-α systems by first treating the upper limits as detections and then setting the upper limits equal to zero. These two approaches yield upper and lower bounds on the averge equivalent width which are plotted in Figure 9 as filled circles. Thus the solid lines connecting the filled circles in Figure 9 represent the range of average absorption-line strength in damped systems in order to aid visual inspections. The number in parentheses after each transition indicates the number of damped connected by dotted lines with the data points for the damped systems in order to aid visual inspections. The number in parentheses after each transition indicates the number of damped systems used in the average for that particular transition. Interestingly, Figure 9 indicates that for most transitions the 3C 273 sight-line measurements fall in or above the range defined by the damped Lyman-α systems. This conclusion is somewhat surprising, in that Lanzetta (1988) and Lu (1991) found from comparing C II λ1334.53 and the C IV doublet absorption lines in damped Lyman-α systems and in Galactic absorption toward the LMC, the SMC, and Galactic halo stars situated at $|z| < 3$ kpc that the damped Lyman-α systems generally show stronger absorption than Galactic sight lines, although trends are only marginally significant. The most notable exceptions to the above observation are for Si II λ1260.42, O I λ1302.17, Si II λ1304.37, and C II λ1334.73, where the absorption in damped Lyman-α systems is about twice as strong as Galactic absorption. The transitions with the largest differences are also the ones that are closest to the Lyman-α line, and are likely to be affected by Lyman-α forest absorption. The fact that the strong low-ionization absorption lines of Fe II, Mg II, and Si II λ1526.71, which almost always occur redward of Lyman-α emission, do not deviate significantly from the range defined by the damped Lyman-α systems lends support for the above interpretation.

The 3C 273 sight line is intermediate in terms of Galactic absorption-line equivalent widths compared with other well-observed Galactic sight lines (Fig. 8). The very strong metal-line absorption characteristics of the 3C 273 sight line approximately correspond to those seen in damped Lyman-α systems (Fig. 9). We tentatively conclude that the strong-line equivalent widths for Galactic disk and halo metal lines are roughly similar to the equivalent widths seen in high-redshift QSO damped Lyman-α systems. Since the low-ionization lines we have compared in Figure 9 are very strong and likely saturated, this correspondence mostly implies a similarity of the kinematical behavior of the turbulent phases of the different absorbing systems and does not imply similar abundances.

6. SUMMARY

The principal results of our study are as follows:

1. We analyze 24 absorption lines found near zero redshift in the GHRS intermediate-resolution spectra of 3C 273 which are attributed to Milky Way disk and halo gas. The reduced

[2] We have intentionally excluded the z = 1.9615 damped system toward QSO 0551 − 366 because of its unusually strong (Δv > 600 km s^{-1}) absorption, which may not be characteristic of most damped systems. The inclusion of this system in the sample significantly affects only the data points of Fe II and Mg II plotted in Fig. 9, owing to the small number of damped Lyman-α systems used in the average.

spectra have a resolution of approximately 20 km s^{-1} (FWHM) with broad wings and a signal-to-noise ratio of 13 to 20.

2. The species detected include C II, C II*, C IV, O I, Mg II, Si II, Si IV, S II, Mn II, Fe II, and Ni II. The O I absorption is blended with Earth atmospheric emission, and one of the Si IV doublet lines is blended with an intergalactic Lyman-α line.

3. Column densities are determined for C II*, C IV, Si II, Si IV, N V, S II, Mn II, and Ni II using standard curve-of-growth techniques and the apparent optical depth method.

4. The column density for S II and a measure of N(H I) from FOS observations of Lyman-α reveal a 45% overabundance of sulfur compared with neutral hydrogen which is probably due to the presence of S II in ionized gas toward 3C 273.

5. The logarithmic depletions for Si, Mn, and Ni are found to be −0.74, −0.67, and −0.81 dex, which are representative of values found for the low-density medium of the Galactic disk.

6. An estimate of the column density of C II* yields a value for the C II cooling rate per nucleon in the gas toward 3C 273 that is 7 times smaller than that found for sight lines through Milky Way disk gas.

7. Reliable column densities for Si IV, C IV, and N V indicate that the amount of highly ionized gas toward 3C 273 perpendicular to the Galactic plane is about 2–4 times greater than that seen toward the LMC and the SMC. The highly ionized gas is most easily understood as being produced by the cooling gas of a Galactic fountain with additional contributions from gas associated with the energetic events that produced Galactic radio loops I and IV.

8. The data provide information about the kinematical behavior of low column density gas at large distances from the Galactic plane. The strongest absorption lines of Fe II, Mg II, Si II, and C II have extensions to positive and negative velocities with full widths at half-absorption strength ranging from ∼120 to ∼150 km s^{-1}. These lines are apparently tracing a high velocity dispersion phase of the neutral gas toward 3C 273.

9. High-velocity absorption-line components, with 100 km $s^{-1} < |v| < 1000$ km s^{-1}, are not evident in the measurements for either the low or the high states of ionization.

10. The observed absorption-line equivalent widths are compared with those for other sight lines through the Milky Way halo, including those to the LMC, the SMC, and the QSO H1821+643. The low-ionization line strengths for the high-latitude direction to 3C 273 are intermediate to those for the SMC and the other two sight lines.

11. The Milky Way disk and halo gas equivalent widths in the strong metal lines toward 3C 273 are compared with the equivalent widths observed in QSO damped Lyman-α systems and found to be similar. The correspondence implies a similarity of the kinematical behavior of the turbulent phases of the different absorbing systems and does not necessarily imply similar elemental abundances.

We express our appreciation to the many technicians, engineers, and scientists who have contributed to the *HST* project. We particularly wish to acknowledge the GHRS PI (John Brandt) and Co-PI (Sally Heap). We appreciate the assistance with the technical aspects of the GHRS reduction software provided by U. J. Sofia, J. Cardelli, and D. Lindler. We thank A. Diplas for determining N(H I) from a profile to the Galactic Lyman-α absorption. A. Davidsen kindly provided the HUT result on O VI absorption in advance of publication. The referee, D. Meyer, provided helpful comments about improving the original manuscript. L. L. and B. D. S. acknowledge support for their involvement in the GHRS through NASA grant NAGW-2520.

REFERENCES

Anders, E., & Grevesse, N. 1989, Geochim. Cosmochim. Acta, 53, 197
Bahcall, J. N., Jannuzi, B. T., Schneider, D. P., Hartig, G. F., Bohlin, R., & Junkkarinen, V. 1991a, ApJ, 377, L5
———. 1991b, in The First Year of *HST* Observations, ed. A. L. Kinney & J. C. Blades (Baltimore: STScI), 46
Bahcall, J. N., Jannuzi, B. T., Schneider, D. P., Hartig, G. F., & Green R. F. 1992, ApJ, 397, 60
Bahcall, J. N., & Spitzer, L. 1969, ApJ, 156, L63
Bergeron, J. 1988, in QSO Absorption Lines: Probing the Universe, ed. J. C. Blades, D. A. Turnshek, & C. A. Norman (Cambridge: Cambridge Univ. Press), 127
Bergeron, J., & Boisse, P. 1991, A&A, 243, 344
Berkhuijsen, E. M. 1971, A&A, 14, 359
———. 1973, A&A, 24, 143
Blades, J. C., & Morton, D. C. 1983, MNRAS, 204, 317
Bohlin, R. C. 1975, ApJ, 200, 402
Brandt, J. C., et al. 1993, in preparation
Burks, G. S., York, D. G., Blades, J. C., Bohlin, R. C., & Wamsteker, W. 1991, ApJ, 381, 55
Coulomb, F. R., Poppel, W. G. L., & Heiles, C. 1980, A&AS, 40, 47
Danly, L. 1989, ApJ, 342, 785
Danly, L., Blades, J. C., & Norman, C. A. 1988, in QSO Absorption Lines: Probing the Universe (Poster Papers), ed. J. C. Blades, D. A. Turnshek, & C. A. Norman (Cambridge: Cambridge Univ. Press), 88
Davidsen, A., Bowers, C. W., Kruk, J. W., Ferguson, H. C., Kriss, G. A., Blair, W. P., & Long, K. S. 1992, in preparation
deBoer, K. S., & Savage, B. D. 1983, ApJ, 265, 210
———. 1984, A&A, 136, L7
Dickey, J. M., & Lockman, F. J. 1990, ARA&A, 28, 215
Duncan, D. K. 1992, Goddard High Resolution Spectrograph Instrument Handbook (Baltimore: STScI)
Ebbets, D. C. 1992, Goddard High Resolution Spectrograph Science Verification Program for the *Hubble Space Telescope*: Final Report (Boulder: Ball Aerospace Group)
Edgar, R. J., & Chevalier, R. A. 1986, ApJ, 310, L27
Fitzpatrick, E. L., & Savage, B. D. 1983, ApJ, 267, 93
Gilliland, R. L., Morris, S. L., Weyman, R. J., Ebbets, D. C., & Lindler, D. J. 1992, PASP, 104, 367
Hartquist, T. W., Pettini, M., & Tallant, A. 1984, ApJ, 276, 519
Heiles, C. 1979, ApJ, 229, 533
Heiles, C., Chu, Y.-H., Reynolds, R. J., Yegingil, I., & Troland, T. H. 1980, ApJ, 242, 533
Hobbs, L. M. 1974, ApJ, 191, 381
Iwan, D. C. 1980, ApJ, 239, 316
Jenkins, E. B. 1978, ApJ, 220, 107
———. 1987, in Interstellar Processes, ed. D. J. Hollenbach & H. A. Thronson, Jr. (Dordrecht: Reidel), 533
Joseph, C., & Jenkins, E. B. 1991, ApJ, 368, 201
Kulkarni, S. R., & Fitch, M. 1985, ApJ, 289, 792
Kulkarni, S. R., & Heiles, C. 1987, in Interstellar Processes, ed. D. J. Hollenbach & H. A. Thronson, Jr. (Dordrecht: Reidel), 87
Lanzetta, K. M. 1988, Ph.D thesis, Univ. Pittsburgh
Lockman, F. J., & Gehman, C. S. 1991, ApJ, 382, 182
Lockman, F. J., Jahoda, K., & McCammon, D. 1986, ApJ, 302, 432
Lockman, F. J., & Savage, B. D. 1993, in preparation
Lu, L. 1991, Ph.D. thesis, Univ. Pittsburgh
Lu, L., & Savage, B. D. 1993, ApJ, submitted
McCammon, D., Burrows, D. N., Sanders, W. T., & Kraushaar, W. L. 1983, ApJ, 269, 107
Meyer, D. M., & Roth, K. C. 1991, ApJ, 383, L41
Morris, S. L., Weymann, R. J., Savage, B. D., & Gilliland, R. L. 1991, ApJ, 377, L21
Morton, D. C. 1975, ApJ, 197, 85
———. 1991, ApJS, 77, 119
Pettini, M., & West, K. 1982, ApJ, 260, 561
Pottasch, S. R., Wesselius, P. R., & van Duinen, R. J. 1979, A&A, 74, L15
Reynolds, R. 1991, in IAU Symp. 144, The Interstellar Disk-Halo Connection in Galaxies, ed. H. Bloemen (Dordrecht: Kluwer), 67
Savage, B. D. 1988, in QSO Absorption Lines: Probing the Universe, ed. J. C. Blades, D. A. Turnshek, & C. A. Norman (Cambridge: Cambridge Univ. Press), 195
Savage, B. D., & deBoer, K. S. 1979, ApJ, 230, L77

Savage, B. D., & deBoer, K. S. 1981, ApJ, 243, 460
Savage, B. D., & Jenkins, E. B., Joseph, C. L., & deBoer, K. S. 1989, ApJ, 345, 395
Savage, B. D., & Jeske, N. A. 1981, ApJ, 244, 768
Savage, B. D., & Massa, D. 1987, ApJ, 314, 380
Savage, B. D., & Sembach, K. 1991, ApJ, 379, 245
Sembach, K., & Savage, B. D. 1992, ApJS, 83, 147
Sembach, K., Savage, B. D., & Massa, D. 1991, ApJ, 372, 81
Shapiro, P. R., & Benjamin, R. A. 1991, PASP, 103, 923
Shapiro, P. R., & Moore, R. T. 1976, ApJ, 207, 406
Spitzer, L. 1990, ARA&A, 28, 71
Spitzer, L., & Fitzpatrick, E. L. 1992, ApJ, 391, L41
Turnshek, D. A., Wolfe, A. M., Lanzetta, K. M., Briggs, F. H., Cohen, R. A., Foltz, C. B., Smith, H. E., & Wilkes, B. J. 1989, ApJ, 344, 567
Wakker, B. P. 1991, in IAU Symp. 144, The Interstellar Disk-Halo Connection in Galaxies, ed. H. Bloemen (Dordrecht: Kluwer), 27
Wolfe, A. M. 1983, ApJ, 268, L1
———. 1988, in QSO Absorption Lines: Probing the Universe, ed. J. C. Blades, D. A. Turnshek, & C. A. Norman (Cambridge: Cambridge Univ. Press), 297
Wolfe, A. M., Turnshek, D. A., Smith, H. E., & Cohen, R. D. 1986, ApJS, 61, 249
York, D. G. 1988, in QSO Absorption Lines: Probing the Universe, ed. J. C. Blades, D. A. Turnshek, & C. A. Norman (Cambridge: Cambridge Univ. Press), 227